Monthly Notices
of the
ROYAL ASTRONOMICAL SOCIETY

MNRAS **479,** 1221–1239 (2018)
Advance Access publication 2018 June 11

doi:10.1093/mnras/sty1465

The unusual ISM in blue and dusty gas-rich galaxies (BADGRS)

L. Dunne,[1,2]★ Z. Zhang,[2,3] P. De Vis,[4] C. J. R. Clark,[1] I. Oteo,[2,3] S. J. Maddox,[1,2] P. Cigan,[1] G. de Zotti,[5] H. L. Gomez,[1] R. J. Ivison,[2,3] K. Rowlands,[6] M. W. L. Smith,[1] P. van der Werf,[7] C. Vlahakis,[8] and J. S. Millard[1]

[1]*School of Physics & Astronomy, Cardiff University, Queens Buildings, The Parade, Cardiff, CF24 3AA, UK*
[2]*SUPA, Institute for Astronomy, University of Edinbugh, Royal Observatory, Blackford Hill, Edinbugh EH9 3HJ, UK*
[3]*ESO, Karl-Schwarzschild-Strasse 2, D-85748 Garching, Germany*
[4]*Institut d'Astrophysique Spatiale, CNRS, Université Paris-Sud, Université Paris-Saclay, Bat. 121, F-91405, Orsay Cedex, France*
[5]*INAF-Osservatorio Astronomico di Padova, Vicolo Osservatorio 5, I-35122, Padova, Italy*
[6]*Johns Hopkins University, Bloomberg Center, 3400 N. Charles St, Baltimore, MD 21218, USA*
[7]*Leiden Observatory, Leiden University, PO Box 9513, NL-2300 RA Leiden, the Netherlands*
[8]*NRAO, 520 Edgemont Road, Charlottesville, VA 22903-2475, USA*

Accepted 2018 June 1. Received 2018 May 10; in original form 2017 December 4

ABSTRACT

The *Herschel*-ATLAS unbiased survey of cold dust in the local Universe is dominated by a surprising population of very blue (FUV-K < 3.5), dust-rich galaxies with high gas fractions ($f_{\rm H\,i} = M_{\rm H\,i}/(M_* + M_{\rm H\,i}) > 0.5$). Dubbed 'Blue and Dusty Gas-Rich Sources' (BADGRS) they have cold diffuse dust temperatures, and the highest dust-to-stellar mass ratios of any galaxies in the local Universe. Here, we explore the molecular interstellar medium in a representative sample of BADGRS, using very deep CO($J_{\rm up} = 1, 2, 3$) observations across the central and outer disc regions. We find very low CO brightnesses ($T_{\rm p} = 5$–30 mK), despite the bright far-infrared emission and metallicities in the range $0.5 < Z/Z_{\odot} < 1.0$. The CO line *ratios* indicate a range of conditions with $R_{21} = T_{\rm b}^{21}/T_{\rm b}^{10} = 0.6 - 2.1$ and $R_{31} = T_{\rm b}^{32}/T_{\rm b}^{10} = 0.2 - 1.2$. Using a metallicity-dependent conversion from CO luminosity to molecular gas mass, we find $M_{\rm H_2}/M_{\rm d} \sim 7 - 27$ and $\Sigma_{\rm H_2} = 0.5$–6 M$_{\odot}$ pc^{-2}, around an order of magnitude lower than expected. The BADGRS have lower molecular gas depletion time-scales ($\tau_{\rm d} \sim 0.5$ Gyr) than other local spirals, lying offset from the Kennicutt–Schmidt relation by a similar factor to Blue Compact Dwarf galaxies. The cold diffuse dust temperature in BADGRS (13–16 K) requires an interstellar radiation field 10–20 times lower than that inferred from their observed surface brightness. We speculate that the dust in these sources has either a very clumpy geometry or a very different opacity in order to explain the cold temperatures and lack of CO emission. BADGRS also have low UV attenuation for their UV colour suggestive of an SMC-type dust attenuation curve, different star formation histories or different dust/star geometry. They lie in a similar part of the IRX-β space as $z \sim 5$ galaxies and may be useful as local analogues for high gas fraction galaxies in the early Universe.

Key words: Galaxies: Local – Infrared – Star-forming – ISM.

1 INTRODUCTION

Blind surveys in unexplored wave-bands often reveal new insights into the process of galaxy evolution, by virtue of a different set of selection characteristics (Schmidt 1963; de Jong et al. 1984; Meegan et al. 1992; Smail, Ivison & Blain 1997; Eales et al. 2018). The Herschel Astrophysical Terahertz Large Area Survey (H-ATLAS: Eales et al. 2010) is the *first blind survey* of the local Universe at sub-millimetre wavelengths (250 μm). In contrast to IRAS, which was only sensitive to the ∼10 per cent (by mass) of dust heated strongly enough to radiate substantially at 60 μm, H-ATLAS selects galaxies based on the ∼90 per cent (by mass) of dust heated to 15–25 K by the diffuse interstellar radiation field (Helou 1986; Dunne et al. 2000; Draine et al. 2007).

Clark et al. (2015) used H-ATLAS to produce the first local volume limited sample selected on the basis of cool dust emission (HAPLESS: $z < 0.01$) and showed that the 250 μm selection probed a uniform range in gas fraction from 10–90 per cent,

★ E-mail: DunneL6@cardiff.ac.uk

in stark contrast to optically selected samples, which are comprised mainly of galaxies dominated by their stellar component. A new population of 'Blue and Dusty Gas-Rich Sources' (henceforth BADGRS) were identified, comprising more than 50 per cent of the 250-μm selected galaxies in HAPLESS. The properties of these BADGRS detailed in Clark et al. (2015) are: very blue UV-NIR colour (FUV − K < 3.5), intermediate stellar mass ($10^8 < M_* < 10^{10}$ $M_\odot$), flocculent or irregular morphologies, and high gas fractions: $f_{\rm H\,I} = M_{\rm H\,I}/(M_* + M_{\rm H\,I}) > 0.5$.[1] For comparison, the average gas fraction for the K-band-selected Herschel Reference Survey (HRS: Boselli et al. 2010) is ∼18 per cent.

Low mass, blue, and gas-rich galaxies are commonly perceived to be low in dust content (Hunter et al. 1989; Giovanelli et al. 1995; Tully et al. 1998); however the BADGRS in H-ATLAS have the highest dust-to-stellar mass ratios of any population in the local Universe (Clark et al. 2015). De Vis et al. (2017a) found that the dust-to-stellar mass ratio peaks at a gas fraction ∼70 per cent, with *BADGRS locating the peak dust content relative to stars and relative to baryons* (however, not relative to gas as this is a monotonically increasing quantity). As these galaxies have only moderate infrared luminosities (8.0 < Log $L_{\rm IR}$ < 10.0), and often low ratios of S_{60}/S_{100}, they are mostly undetected or very faint in the IRAS bands. A wide area, sensitive sub-millimetre survey such as H-ATLAS was therefore required to identify this population. In addition to making up more than half the number density of sub-mm galaxies in the local volume, BADGRS account for 30 per cent of the integrated dust mass density and 20 per cent of the star formation rate (SFR) density in the volume probed by HAPLESS, yet contain only 6 per cent of the stellar mass (Clark et al. 2015).

De Vis et al. (2017b) used chemical and dust evolution modelling to show that different processes must be acting in either the formation or destruction of dust at the same gas fraction in order to explain the differences between BADGRS and the more commonly studied dust-poor, metal-poor, gas-rich galaxies in the Herschel studies of H I-selected (HIGH: De Vis et al. 2017a) and dwarf galaxies (DGS: Madden et al. 2013). BADGRS may therefore be a Rosetta Stone for understanding the changes in both the dust and gas properties of the interstellar medium (ISM) when it becomes enriched with dust, yet is still dominated by gas rather than stars (a situation which will be more common in the early universe).

Fig. 1(a) shows the dust content relative to stellar mass versus the gas fraction for sources from the dust (HAPLESS), H I (HIGH), and K-band (HRS) selected samples (Boselli et al. 2010; Clark et al. 2015; De Vis et al. 2017a). Blue circles represent those HAPLESS and HIGH sources with FUV − K < 3.5 that are in the H-ATLAS catalogue. The remaining HAPLESS sources with redder colours are shown as green circles, and HIGH sources that are not in the H-ATLAS catalogues are red open circles. The K-band-selected HRS galaxies are shown in grey; the nature of their K-band selection ensures that most are evolved and gas poor (residing at the right of the plot). The FUV − K < 3.5 dust detected sources (blue circles) are mostly located in a region in the upper left quadrant of this parameter space – i.e. they are both dust and gas rich. The few exceptions are early-type galaxies at lower gas fraction undergoing interactions with gas-rich galaxies, and two low dust mass sources at high gas fraction which are the very local dwarf galaxies UM451 and UM452. We now make the working definition of 'Blue and Dusty Gas-Rich Sources' (BADGRS) to be (FUV − K < 3.5) *and* (Log $M_{\rm d}/M_* > -2.46 - \log(\kappa_{250}/0.56)$), this consists of the blue points contained within the shaded box in Fig. 1(a). Fig. 1(b) shows the relation between dust mass and SFR (normalized by stellar mass to remove the tendency for large galaxies to have more of everything). This correlation has been found to hold for local galaxies and SMGs at high redshift (da Cunha et al. 2010; Smith et al. 2012a; Rowlands et al. 2014). BADGRS from the HIGH and HAPLESS samples are denoted as cyan squares, while the individual regions for our four pilot targets are shown as blue circles. BADGRS have more dust per unit SFR than similarly high sSFR galaxies which do not meet the colour and dust content threshold.

BADGRS possess common properties which are intriguing and indicate an unusual ISM:

(i) *Hot but cold:* Their diffuseed ISM dust temperatures are far colder (12–16K) than the average for spirals and dwarfs (18–32K), despite their relatively intense UV emission (Clark et al. 2015).

(ii) *Blue but dusty:* They have very little UV obscuration compared to other galaxies with similar dust masses, or similar UV colours (De Vis et al. 2017a, Dunne et al. in preparation).

(iii) *Metal rich but CO poor:* We found that their predicted CO luminosities were far lower than expected given their dust emission, assuming they lay on the M_*–$M_{\rm H2}$ scaling relations of local galaxies (e.g. Saintonge et al. 2011; Bothwell et al. 2014).

It was this final puzzle which led us to propose extremely sensitive CO observations with the IRAM 30-m telescope in order to test whether these galaxies were indeed unusually rich in dust and IR emission relative to their molecular gas content. This first paper motivates the case for an unusual ISM in BADGRS by presenting our first complete data set of ^{12}CO(1 − 0), ^{12}CO(2 − 1), and ^{12}CO(3 − 2) measurements in nine regions across four representative examples of BADGRS from Clark et al. (2015). We compare the CO properties to those of the dust (as traced by *Herschel*) in the same regions. We will also investigate the dust heating and obscuration puzzles and their potential relationship to the CO observations.

In Sections 2.1 and 2.2, we describe the sample and CO observations. In Section 3, we discuss the CO and molecular gas properties. In Section 4, we describe the dust properties and compare those of other samples from the literature. In Section 5, we discuss the ISM of BADGRS and look for possible explanations for their unusual properties. Throughout we use a cosmology with $\Omega_{\rm m} = 0.27$, $\Omega_\Lambda = 0.73$, and $H_o = 71$ km s^{-1} Mpc^{-1}.

2 SAMPLE AND DATA

2.1 The pilot sample of BADGRS

To undertake an initial detailed study of BADGRS, we selected a small pilot sample which was representative of the group. The very local (D < 45 Mpc) nature of the sources in Clark et al. (2015) means they typically have large angular sizes making a detailed study of the dust, gas, and optical properties in a large sample prohibitive. We chose four galaxies which spanned the range in stellar mass, gas fraction, colour (FUV-K), and morphology seen across the BADGRS population and which were bright enough and resolved enough to provide excellent targets for follow up. Fig. 1(a) shows our pilot sample as blue circles surrounding blue dots, and Table 1 summarizes their global properties.

The FIR data set used for the *Herschel*-ATLAS local volume sample and this paper is the H-ATLAS DR1 release described in Valiante et al. (2016) and Bourne et al. (2016). It consists of imaging in five bands from 100–500 μm, covering the 161 sq deg of H-

[1] See Clark et al. (2015) and De Vis et al. (2017a) for details of the H I data.

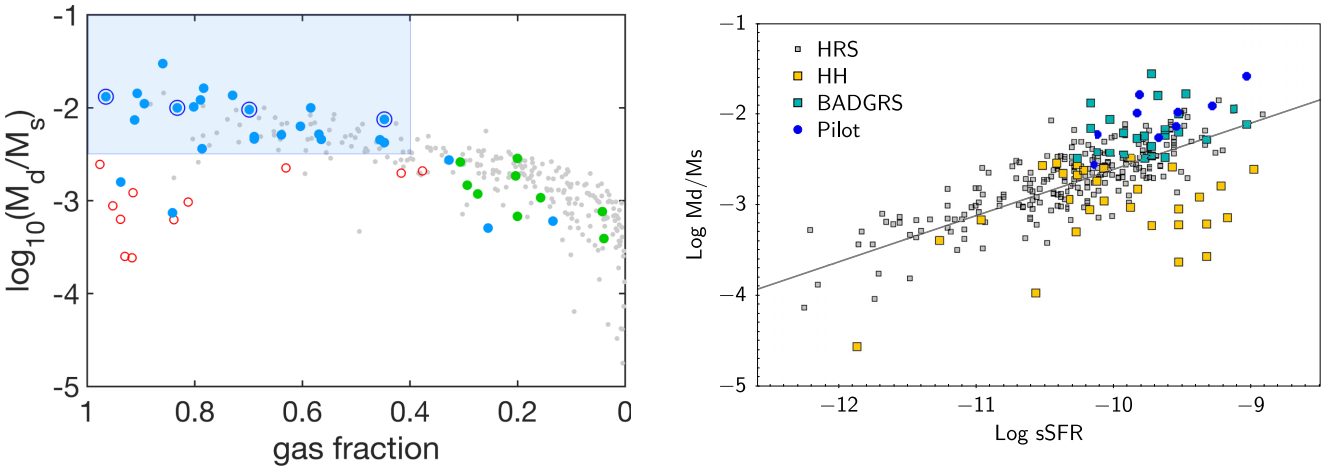

Figure 1. *Left*: Specific dust mass (M_d/M_*) versus gas fraction for local galaxy samples. Galaxies with FUV − K < 3.5 and which are detected in H-ATLAS are denoted by blue circles. The parent samples are the dust-selected local volume sources from Clark et al. (2015) and the H I-selected sample from De Vis et al. (2017a). Dust- and HI-selected sources from the parent samples which do not have both the blue colour and H-ATLAS detections are shown as filled green and red open circles, respectively. The shaded box indicates our definition of BADGRS as described in the text. Our CO BADGRS sample is highlighted by dark blue circles surrounding the points. K-band-selected sources (grey) are from HRS (Boselli et al. 2010). Dust masses are all scaled to $\kappa_{250} = 0.56\,\mathrm{m^2\,kg^{-1}}$ and are determined in an equivalent way, using either MAGPHYS or two temperature MBB fitting. For more information on dust mass determination, see Section 4. *Right*: Dust mass versus SFR (normalized by stellar mass). BADGRS have more dust per unit SFR than typical galaxies and the wide spread of dust per SFR is apparent at high sSFR due to the inclusion of the HI-selected, dust-poor sources from HIGH (De Vis et al. 2017a). BADGRS from both HIGH and HAPLESS are shown in cyan while the individual regions of the pilot sample presented here are blue circles. Gold squares are the HIGH and HAPLESS sources which do not meet the BADGRS criteria of being blue *and* dusty.

Table 1. Properties of the four BADGRS in our pilot sample.

Name	$v_{\rm lsr}$ ($\mathrm{km\,s^{-1}}$)	D (Mpc)	Log M_* ($\mathrm{M_\odot}$)	Log μ_* ($\mathrm{M_\odot\,kpc^{-2}}$)	Log $\mathrm{L_{IR}}$ ($\mathrm{L_\odot}$)	Log $M_{\rm d}$ ($\mathrm{M_\odot}$)	Log $M_{\rm HI}$ ($\mathrm{M_\odot}$)	FUV-K	sSFR log ($\mathrm{yr^{-1}}$)	$f_{\rm HI}$
NGC 5584	1638	30.2	9.98	7.02	10.04	7.80	9.76	2.68	−9.71	0.44
NGC 5496	1541	27.4	9.46	6.64	9.51	7.53	10.03	2.34	−9.62	0.83
UGC 9215	1397	25.6	9.31	6.93	9.57	7.28	9.56	2.06	−9.47	0.70
UGC 9299	1539	28.3	8.61	6.67	8.82	6.74	9.94	0.93	−9.20	0.97

$v_{\rm lsr}$ is the recessional velocity. Distance is taken from De Vis et al. (2017a) and is local flow corrected following Baldry et al. (2012), M_* and $\mathrm{L_{IR}}$ from MAGPHYS (De Vis et al. 2017a), $M_{\rm d}$ from two-temperature MBB fit, $M_{\rm HI}$ for NGC 5584 and NGC 5496 from HIPASS (Meyer et al. 2004), and for UGC 9215 and UGC 9299 from ALFALFA (Haynes et al. 2011), SFR is from UV+TIR following equation (1). $f_{\rm HI} = M_{\rm HI}/(M_* + M_{\rm HI})$. $M_{\rm HI}$ includes a factor 1.36 to account for He.

ATLAS which coincides with the equatorial fields of the Galaxy And Mass Assembly (GAMA; Driver et al. 2011) survey. The FUV-22- μm imaging was provided by GAMA (Driver et al. 2016), who consolidated the data from multiple public surveys into a format ideal for multiband matched-aperture photometry. The photometry was performed as described in Clark et al. (2015) and De Vis et al. (2017a). Optical spectra of the central region, and some H II regions were taken from GAMA and SDSS (Hopkins et al. 2013; Ahn et al. 2014) and used to provide redshifts and estimate metallicities. Composite colour images of the galaxies are shown in Fig. 2, their semimajor axis size ranges from 1.5 to 5 arcmin, and they have inclinations in the range 50–80 deg.

The galaxies were observed using nine pointings with the IRAM 30-m and APEX[2] to probe the properties of the molecular gas across the central and disc regions. The regions sampled are shown in Fig. 2 and the positions are listed in Table 2. The positions are named such that the central position is 'C' and the offset positions are 'O1,O2'. At the distance of the galaxies, the 22 arcsec beam of the IRAM 30-m at 115-GHz corresponds to 2–3 kpc linear size.

[2]This publication is based on data acquired with the Atacama Pathfinder Experiment (APEX). APEX is a collaboration between the Max-Planck-Institut fur Radioastronomie, the European Southern Observatory, and the Onsala Space Observatory.

Atomic gas properties

The very blue FUV − K < 3.5 sources in the HAPLESS (Clark et al. 2015) sample have a high average $f_{\rm HI} = 0.66$, due to the correlation between FUV − K colour, sSFR and gas content. Our additional dust content selection criteria (Fig. 1a) makes the BADGRS sample exclusively gas rich. The global atomic gas fractions for the pilot sample are listed in Table 1. The H I measurements (presented in Clark et al. 2015; De Vis et al. 2017a) are from single dish surveys with the Parkes (HIPASS; Meyer et al. 2004) and Arecibo (ALFALFA; Haynes et al. 2011) telescopes and as such have poor angular resolution ranging from 5 to 15 arcmin. This means that apart from a global measure of their atomic gas content, we can do no more at this time to explore the relationship between the dust, molecular and atomic gas content as the dust and molecular gas are observed with 2–3 kpc angular resolution in the galaxy discs while a large fraction of the HI could reside at much larger radii, as is

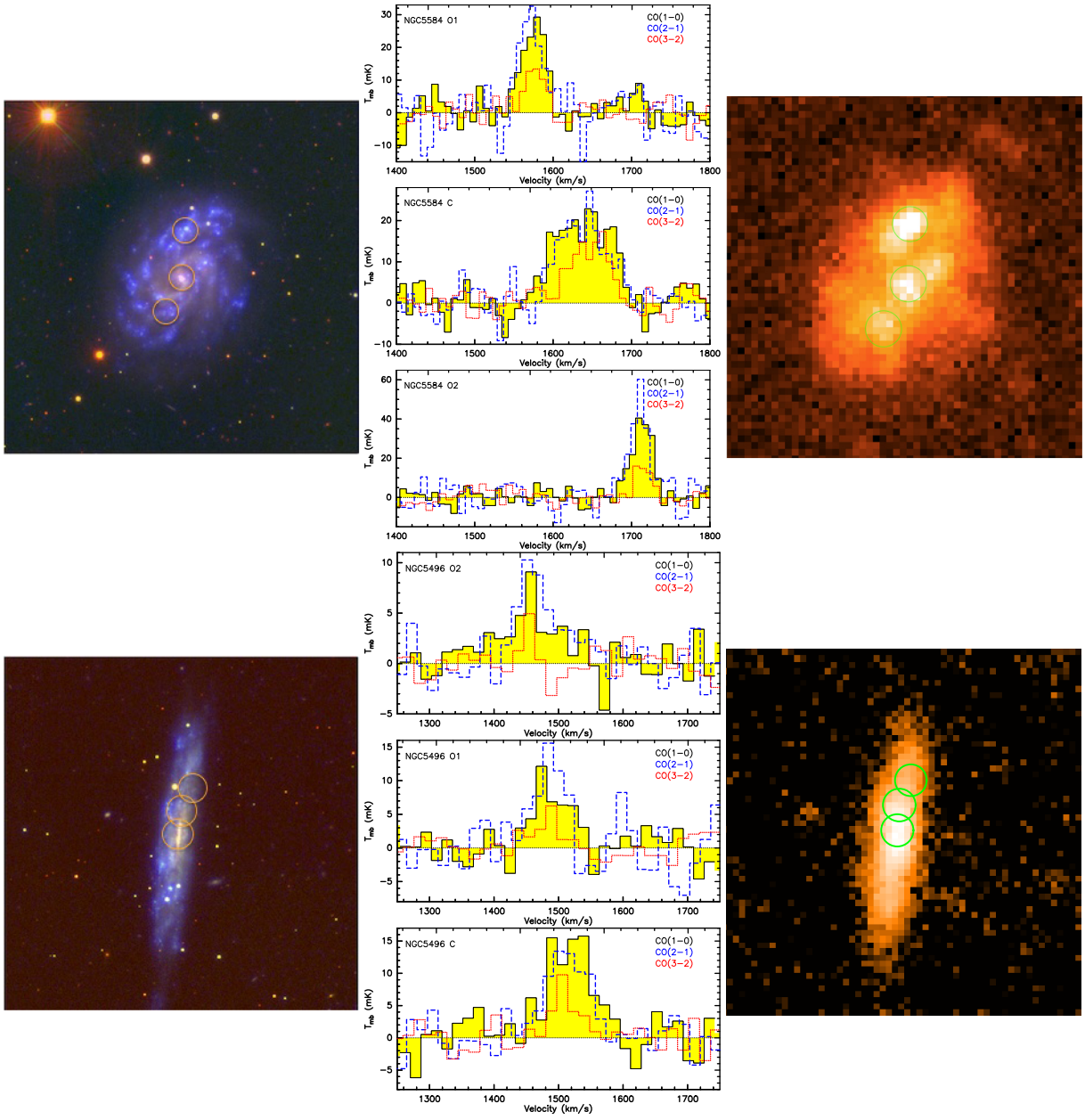

Figure 2. *Left:* NUV/r/Z composite image of NGC 5584 (top) and NGC 5496 (bottom) with the CO pointings shown in yellow, representing the FWHM of the ^{12}CO(1 − 0) beam (22 arcsec). *Centre:* Spectra on the $T_{\rm mb}$ scale for each pointing, all three transitions are included in each panel. *Right:* The 250 μm image (un-smoothed) with the CO pointings shown. *Left:* NUV/r/Z composite image of UGC9215 (top) and UGC9299 (bottom) with the CO pointings shown in yellow, representing the FWHM of the ^{12}CO(1 − 0) beam (22 arcsec). *Centre:* Spectra on the $T_{\rm mb}$ scale for each pointing, all three transitions are included in each panel. *Right:* The 250-μm image (un-smoothed) with the CO pointings shown.

common for lower surface brightness blue galaxies such as these. A future study (Dunne et al. in preparation) will investigate the atomic gas properties in detail using higher resolution interferometric HI data.

Metallicities

There are local metallicity estimates for all of our gas and dust comparisons, as for each CO pointing there is at least one metallicity measure available within the 115-GHz beam area of the IRAM 30 m. For NGC 5496, UGC 9215 and UGC 9299 metallicities were taken from De Vis et al. (2017b), who used the SDSS and GAMA spectra and strong line ratios, and are quoted in the Pettini & Pagel (2004) O3N2 calibration. There are 10 measurements in total across the 6 CO pointings, as several H II regions were observed in some galaxies. For NGC 5584, we use the comprehensive set of measurements as part of the *HST* Cepheid study by Riess et al. (2011), which results in 14 metallicity measures across the three pointings. We convert the metallicity calibration used in Riess et al. (2011) to the O3N2 relation using the conversions given by Kewley & Ellison (2008). The local metallicity measures match the recent determination of the $\Sigma_* - Z$ relation using the MaNGA survey (Barrera-Ballesteros et al. 2016). Metallicities for each region are listed in Table 4 and range from $12 + \log({\rm O/H}) = 8.3 - 8.7$ ($0.4-1\,{\rm Z}_\odot$), with an aver-

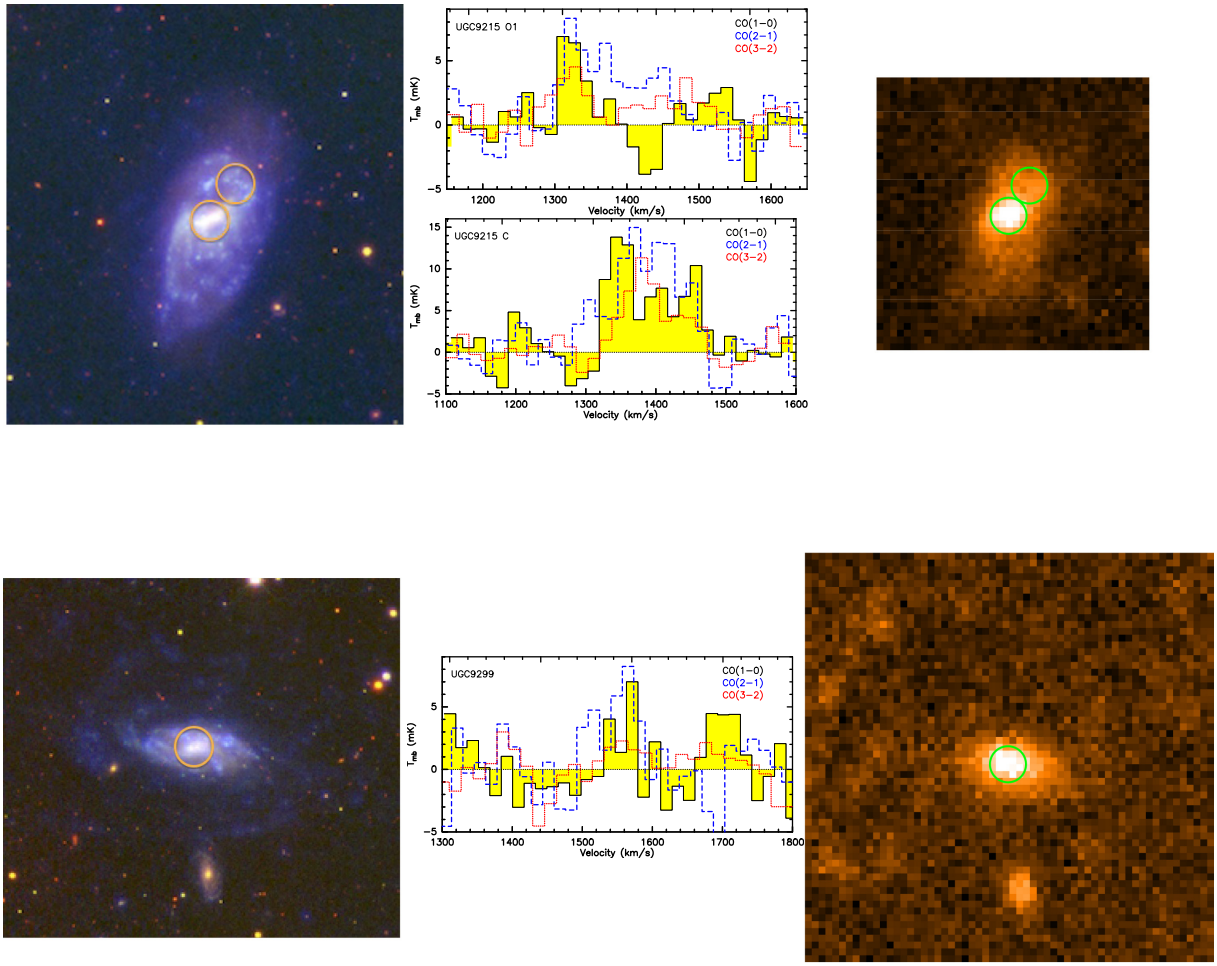

Figure 2. continue

age of 8.51 (0.66 $Z_{\odot}$), assuming $12 + \log(O/H)_{\odot} = 8.67$ (Asplund et al. 2009).

Global properties

Stellar masses, infrared luminosities, and global FUV attenuations are taken from De Vis et al. (2017a), who used MAGPHYS, an energy balance SED-fitting code (da Cunha, Charlot & Elbaz 2008), and 21-band matched aperture photometry measurements from FUV-500μm. We estimate the recent SFR using the relation (Hao et al. 2011; Kennicutt & Evans 2012)

$$\mathrm{Log\,SFR} = \mathrm{Log}(\mathrm{L_{FUV}} + \eta\ \mathrm{L_{IR}}) - 43.35 \quad (1)$$

with luminosities in units of erg s^{-1}. The parameter η describes the contribution of dust heated by young stars to the L_{IR} and we take the value of $\eta = 0.46$ from Hao et al. (2011). Comparing the total SFR to that traced by the uncorrected FUV gives us unobscured SFR fractions of 53, 64, 58, and 81 per cent for the four sources, respectively.[3]

[3]The MAGPHYS SFR PDFs for these very blue galaxies were often multipeaked meaning the median value was not a good representation of the most likely SFR value. See De Vis et al. (2017a); Schofield (2017) for details.

We have used the original two component modified blackbody method of deriving the dust properties, as presented in Clark et al. (2015) and described originally in Dunne & Eales (2001) because MAGPHYS consistently underpredicts the 500 μm flux for all the sources which show cold dust temperatures in Clark et al. (2015). We believe this is due to some of the complex priors used in the energy balance and infrared SED construction in MAGPHYS. More details of the dust SED fitting are given in Section 4.

These global properties are listed in Table 1.

2.2 CO observations

Observations of the ^{12}CO(1 − 0) and ^{12}CO(2 − 1) lines were made with the IRAM 30-m telescope between 2014 July 2 and July 4. The EMIR spectrometer was used, combining the E090 and E230 dichroics which allowed simultaneous observations of both ^{12}CO lines, and additionally the ^{13}CO(1 − 0) line. The beam sizes are 21.5 arcsec and 10.7 arcsec, respectively. The WILMA back-end was used, producing a frequency resolution of 0.51 MHz, which was then hanning smoothed in data analysis to typically 8–16km s^{-1}. Wobbler switching with a throw of 240 arcsec, large enough to be off the target galaxy, was used. The opacity at 225 GHz ranged from 0.09 to 0.6 over the three nights with p.w.v. of 1.5–3 mm. Each scan lasted 4.8 min, producing total integration times of 57–211 min per pointing. The spectra were reduced using the GILDAS–CLASS software

Table 2. Details of the CO measurements.

Pointing	R.A. (J2000)	Dec (J2000)	v_{10} (km s^{-1})	I_{10} (K km s^{-1})	Δv_{10} (km s^{-1})	σ_{10} (mK)	$^{13}I_{10}$ (K km s^{-1})	I_{21} (K km s^{-1})	Δv_{21} (km s^{-1})	σ_{21} (mK)	I_{32} (K km s^{-1})	Δv_{32} (km s^{-1})	σ_{32} (mK)
NGC 5584 C	14:22:23.6	−00:23:14	1636	2.11 ± 0.15	86	2.6	<0.16	1.54 ± 0.14	71	2.6	0.81 ± 0.11	53	2.6
NGC 5584 O1	14:22:23.5	−00:22:28	1573	1.07 ± 0.11	35	4.8	<0.11	1.04 ± 0.14	31	6.0	0.42 ± 0.07	28	3.5
NGC 5584 O2	14:22:24.8	−00:23:46	1710	1.48 ± 0.11	32	4.5	<0.11	1.39 ± 0.15	23	6.7	0.43 ± 0.07	23	4.0
NGC 5496 C	14:11:37.8	−01:09:24	1515	1.17 ± 0.15	73	3.1	0.28 ± 0.06	1.03 ± 0.16	71	3.0	0.45 ± 0.09	47	1.9
NGC 5496 O1	14:11:37.7	−01:09:03	1474	0.69 ± 0.09	57	2.8	<0.14	0.82 ± 0.19	49	4.4	0.32 ± 0.07	50	1.6
NGC 5496 O2	14:11:37.0	−01:08:43	1456	0.63 ± 0.15	100	1.8	<0.11	0.63 ± 0.12	59	2.5	0.12 ± 0.03	23	1.3
UGC9215 C	14:23:27.3	+01:43:34	1382	1.21 ± 0.17	87	3.2	<0.21	1.35 ± 0.12	90	2.5	0.78 ± 0.09	64	1.6
UGC9215 O	14:23:26.3	+01:43:56	1319	0.33 ± 0.07	44	1.8	<0.09	0.64 ± 0.11	75	2.0	0.23 ± 0.06	51	1.5
UGC9299	14:29:34.6	−00:01:06	1550	0.15 ± 0.07 (<0.239)[a]	22 (69)[a]	2.4	<0.12	0.47 ± 0.09 (0.31 ± 0.10)[b]	59 (36)[b]	2.2	0.20 ± 0.08	75	1.5

All intensity units are in the $T_{\rm mb}$ scale. v_{10} is the central velocity of the ^{12}CO(1 − 0) line in the LSRK frame. $I_{\rm CO}$ is the integrated intensity $\int T_{\rm mb}\delta v$. $\Delta v_{\rm CO}$ is the FWHM of the CO line as given by equation (2). $\sigma_{\rm CO}$ is the spectral rms in the binned spectrum . [a]Measurement for UGC9299 made in three channels corresponding to the peak in ^{12}CO(2 − 1) and ^{12}CO(3 − 2). Upper limit for UGC9299 from integrating across the FWZI of the main peak in the ^{12}CO(2 − 1) line. [b] ^{12}CO(2 − 1) flux for UGC9299 measured in the same velocity range as ^{12}CO(1 − 0) and ^{12}CO(3 − 2). Larger measurement not in parenthesis includes the blue-ward peak, which is not evident in the other two lines.

(Pety 2005),[4] noisy channels were flagged and replaced with the local noise from the channels either side and a first-order baseline was subtracted from each individual scan. Scans were then averaged using a $t/T_{\rm sys}^2$ weighting and smoothed to the desired velocity resolution. A linear baseline was then subtracted from the averaged spectrum and the resultant velocity integrated line intensity (moment 0) was measured between the FWZI points. Units of intensity were converted from the $T_{\rm A}^*$ scale to $T_{\rm mb}$ using the values in the IRAM 30-m report (Kramer, Penalver & Greve 2013)[5] of $F_{\rm eff} = 0.94,\ 0.92$ and $B_{\rm eff} = 0.78,\ 0.59$ at 115, 230 GHz, respectively. This gives conversions of $T_{\rm mb} = 1.205\,T_{\rm A}^*$ at 115 GHz and $T_{\rm mb} = 1.559\,T_{\rm A}^*$ at 230 GHz.

The line-widths (FWHM) were calculated as follows (Heyer, Carpenter & Snell 2001; Leroy et al. 2016)

$$\Delta v_{\rm CO} = 2.35\frac{I}{\sqrt{2\pi}\,I_{\rm p}}, \tag{2}$$

where I is the integrated intensity and $I_{\rm p}$ the peak intensity. This method is less prone to error than Gaussian fitting or moment based methods.[6] Where a line was not detected we report the 3σ upper limit as

$$I_{\rm CO} < 3\sigma\,\sqrt{\Delta v_{\rm CO}\delta v}$$

with σ being the spectral rms in mK, $\Delta v_{\rm co}$ the line-width expected and δv the channel width in km s^{-1}.

Observations of the ^{12}CO(3 − 2) line were made with the APEX 12-m telescope between 2015 April and July. The beam-size at 352 GHz is 17.3 arcsec . The APEX-2 front-end was used with the XFFTS back-end, resulting in an instrumental velocity resolution of 0.0665km s^{-1}, which was then hanning smoothed to 8–17 km s^{-1}. The weather was good with precipitable water vapour ranging from 0.4 to 1.3 mm. On source integration times ranged from 16–62 mins, resulting in typical rms of 1.4 mK in a 30km s^{-1} channel.

The spectra were reduced with CLASS in the same way as described above for the IRAM 30-m, and the intensity units converted from $T_{\rm A}^*$ to $T_{\rm mb}$ using values of $\eta_f = 0.97$ and $\eta_{\rm mb} = 0.73$ at 352 GHz, resulting in a conversion of $T_{\rm mb} = 1.329\,T_{\rm A}^*$

The integrated line intensities and other observational parameters are listed in Table 2 and the spectra are shown in Fig. 2.

The line intensities were converted to fluxes using the appropriate Jy K^{-1} conversion factors: $S_\nu/T_{\rm mb}$= 5.0 Jy K^{-1} for ^{12}CO(1 − 0), 5.01 Jy K^{-1} for ^{12}CO(2 − 1), and 30.85 Jy K^{-1} for ^{12}CO(3 − 2). The fluxes are listed in Table 3.

3 CO AND MOLECULAR GAS PROPERTIES

The CO measurements in Tables 2 and 3 are used to provide diagnostics of the molecular gas in the nine regions of the four targets. The integrated line flux density gives a measure of the molecular gas in the beam in$M_\odot$, as $M_{\rm H_2} = \alpha_{\rm CO}\,L'_{10}$, where L'_{10} is given by

$$L'_{10} = 3.25\times10^7\,S_{10}\,\nu_{\rm obs}^{-2}\,D_{\rm L}^2\,(1+z)^{-3}\ {\rm K\,kms^{-1}\,pc^{-2}} \tag{3}$$

where S_{10} is the integrated CO(1–0) flux density in Jykm s^{-1}, $\nu_{\rm obs}$ is the observed frequency of the emission line in GHz, $D_{\rm L}$ is the luminosity distance in Mpc and z is the redshift.

[4] http://www.iram.fr/IRAMFR/GILDAS/

[5] http://www.iram.es/IRAMES/mainWiki/CalibrationPapers

[6] Where the SNR was high enough and Gaussians could be fitted, we found excellent agreement between the fitted FWHM and the method above.

Table 3. Flux densities and line ratios of the molecular gas.

Pointing	S_{10} (Jy km s^{-1})	S_{21} (Jy km s^{-1})	S_{32} (Jy km s^{-1})	C_{21}	C_{31}	R_{21}	R_{31}	R_{10}
N5584 C	10.53 ± 0.75	7.69 ± 0.70	24.9 ± 3.4	0.794	0.934	0.58 ± 0.07	0.36 ± 0.05	>13.2
N5584 O1	5.37 ± 0.55	5.20 ± 0.70	12.8 ± 2.2	0.676	0.877	0.66 ± 0.11	0.34 ± 0.07	>9.7
N5584 O2	7.4 ± 0.55	6.94 ± 0.75	13.1 ± 2.2	0.847	0.943	0.80 ± 0.10	0.27 ± 0.05	>13.5
N5496 C	5.87 ± 0.75	5.16 ± 0.80	13.8 ± 2.8	0.872	0.943	0.77 ± 0.15	0.36 ± 0.09	4.2 ± 1.1
N5496 O1	3.47 ± 0.45	4.09 ± 0.95	9.8 ± 2.2	0.943	0.943	1.12 ± 0.30	0.44 ± 0.11	>4.9
N5496 O2	3.20 ± 0.75	3.17 ± 0.60	3.7 ± 0.9	1.00	1.00	1.00 ± 0.30	0.19 ± 0.07	>5.7
U9215 C	6.05 ± 0.85	6.74 ± 0.60	24.1 ± 2.8	0.637	0.820	0.71 ± 0.12	0.53 ± 0.10	>5.8
U9215 O1	1.65 ± 0.35	3.21 ± 0.55	6.82 ± 1.9	1.087	1.08	2.11 ± 0.58	0.75 ± 0.25	>3.7
U9299	0.77 ± 0.35 (<1.2)	1.54 ± 0.50 (2.33 ± 0.75)	6.2 ± 2.5	0.719	0.877	1.49 ± 0.84 (>0.93)	1.17 ± 0.72 (>0.73)	...

$S_\nu/T_{\rm mb}$ used are: 5.0 Jy K^{-1} for ^{12}CO(1 − 0), 5.01 Jy K^{-1} for ^{12}CO(2 − 1), and 30.85 Jy K^{-1} for ^{12}CO(3 − 2). R_{21} and R_{31} are the integrated line temperature ratios of the ^{12}CO(2 − 1)/^{12}CO(1 − 0) and ^{12}CO(3 − 2)/^{12}CO(1 − 0) lines, respectively. R_{21} and R_{31} have been corrected for the mismatched beam sizes using the multiplicative factors C_{21} and C_{31} as described in the text. R_{10} is the ratio of $^{12}I_{10}/^{13}I_{10}$.

Table 4. Dust and molecular gas masses.

Pointing	S_{250} (CO) (Jy)	S_{250} (tot) (Jy)	$T_{\rm c}$ (K)	$M_{\rm d}$(tot) (Log M$_\odot$)	$M_{\rm d}$(CO) (Log M$_\odot$)	12 + log(O/H)	α_Z	$M_{\rm H_2}$ (Log M$_\odot$)	$M_{\rm H_2}/M_{\rm d}$
N5584 C	0.402	5.880	13.8 ± 1.2	7.80 ± 0.06	6.63	8.69 (3)	4.3	8.00 (8.00)	23 (23)
N5584 O1	0.445				6.68	8.52 (7)	6.0	7.71 (7.85)	11 (16)
N5584 O2	0.336				6.56	8.64 (4)	4.3	7.85 (7.85)	19 (19)
N5496 C	0.500	2.513	13.0 ± 0.7	7.53 ± 0.05	6.83	8.63 (1)	4.3	7.67 (7.67)	7 (7)
N5496 O1	0.374				6.70	8.34 (4)	10.3	7.44 (7.82)	5 (13)
N5496 O2	0.165				6.35	8.32 (1)	10.4	7.40 (7.78)	11 (27)
U9215 C	0.492	2.000	13.8 ± 1.4	7.28 ± 0.10	6.67	8.44 (1)	8.0	7.62 (7.89)	9 (17)
U9215 O1	0.219				6.32	8.36 (2)	10.1	7.06 (7.42)	5 (13)
U9299	0.184	0.560	14.6 ± 0.7	6.74 ± 0.05	6.26	8.47	7.0	7.00 (7.21)	6 (9)

S_{250}(CO) is the 250- μm flux in the area of the 115-GHz IRAM beam. $T_{\rm c}$ is the cold dust temperature from the two component MBB fit. $M_{\rm d}$(tot) is the total dust mass using the aperture 250- μm flux and the two component SED fit. $M_{\rm d}$(CO) is the inferred dust mass using S_{250}(CO) and the global SED parameters. We use a dust mass opacity coefficient of $\kappa_{250} = 0.56\,{\rm m^2 kg^{-1}}$ from Planck Collaboration XIX (2011). Metallicities are taken from De Vis et al. (2017b) and Riess et al. (2011) and are quoted in the O3N2 calibration of Pettini & Pagel (2004). The number of H II regions which have been averaged to get this metallicity are in parentheses. $\alpha_{\rm CO}$ is chosen to be either the MW value of 4.3 M$_\odot$(K km s^{-1}pc^{-2})$^{-1}$ or a metallicity-dependent value listed as α_Z taken from Wolfire et al. (2010). All $\alpha_{\rm CO}$ include the contribution from He. $M_{\rm H_2}$ values using α_Z are in parentheses following those derived from the MW $\alpha_{\rm CO}$ value.

The conversion factor from CO luminosity to H_2 mass, $\alpha_{\rm CO}$, is known to be sensitive to metallicity (Wolfire, Hollenbach & McKee 2010; Glover & Mac Low 2011; Leroy et al. 2011; Papadopoulos et al. 2012; Bolatto, Wolfire & Leroy 2013) although it is not extremely sensitive for $Z > 0.5\,Z_\odot$ which applies to all of our galaxies. To consider the impact of metallicity effects, we make two estimates of $M_{\rm H_2}$ for each region. For the first we use the Milky Way value of $\alpha_{\rm CO} = 4.3\,{\rm M_\odot\,(K\,km\,s^{-1}pc^{-2})^{-1}}$ (including He) from Bolatto et al. (2013), thus giving each region the same CO–H_2 relation. Secondly, we use the metallicity-dependent $\alpha_{\rm CO}$ of Wolfire et al. (2010).[7] This provides a unique scaling for each region based on its local metallicity.

In general, the CO emission is very weak with low peak temperatures [5–30 mK ($T_{\rm mb}$) and narrow line-widths].[8] In particular, the most massive galaxy, NGC 5584, has very narrow lines in the outer regions of the disc (FWHM ∼ 20–30km s^{-1}). Since the regions probed by the ^{12}CO(1 − 0) beam are 2–3 kpc in diametre, such narrow lines indicate that the CO is likely to be in small clouds with narrow intrinsic line-widths. The implied molecular gas surface density (including He) averaged over these 2–3 kpc regions ($\Sigma_{\rm H_2,CO} = \alpha_{\rm CO}\,I_{\rm CO}\,\cos i$) is $\Sigma_{\rm H_2} \sim 0.5 - 6\,{\rm M_\odot\,pc^{-2}}$. This is 6−10× lower than the density of *inter-arm* gas in M51 averaged over a similar area (Colombo et al. 2014). The values of $\Sigma_{\rm H_2,CO}$ for the individual pointings are listed in Table 5.

3.1 Line ratios

The line luminosity or brightness temperature ratio provides some diagnostic of the excitation of the molecular gas *averaged over the beam area*. For a point source sampled with the same beam size in both transitions, or a very extended source, this is equivalent to the ratio of line integrated intensities in $T_{\rm mb}$ units, such that

[7] We also checked that using the $\alpha_{\rm CO}$(Z) of Feldmann, Hernandez & Gnedin (2012), Glover & Mac Low (2011), or Genzel et al. (2015) did not change any of our conclusions: of all the relations, the Wolfire et al. (2010) $\alpha_{\rm CO}$ gave the maximum $M_{\rm H_2}$ at a given metallicity.

[8] Two of these galaxies (NGC 5584 and NGC 5496) were also observed with the JCMT in the ^{12}CO(2 − 1) and ^{12}CO(3 − 2) lines by Bourne et al. (2013). The noise levels in the JMCT data were considerably higher but the results are consistent with our newer and deeper observations.

Table 5. CO and dust-based gas surface densities and ISM pressure.

Pointing	$\Omega_{\rm beam}$	i	$\Sigma_{\rm H_2,CO}$	$\Sigma_{\rm d,0}$	G/D	$\Sigma_{\rm g,0}$	$\Sigma_{*,0}$	$P_{\rm ext}/k$	$f_{\rm H_2,th}$	$\frac{f_{\rm H_2,th}}{f_{\rm H_2,CO}}$
	(kpc^2)		($M_\odot$ pc^{-2})	($M_\odot$ pc^{-2})		($M_\odot$ pc^{-2})	($M_\odot$ pc^{-2})	(10^4 K cm^{-3})		
N5584 C	11.3	56[1]	5.1	0.21	154	32.3	76.2	11.7	0.8	5
N5584 O1	...	...	3.6	0.23	228	52.3	8.8	10.6	0.7	10
N5584 O2	...	...	3.6	0.18	173	31.1	17.0	5.0	0.6	5
N5496 C	9.3	79[2]	1.0	0.14	177	24.2	22.7	3.8	0.6	15
N5496 O1	...	...	1.4	0.11	344	37.8	9.7	6.0	0.5	13
N5496 O2	...	...	1.2	0.05	361	16.9	4.5	1.2	0.2	3
U9215 C	8.1	54[1]	5.7	0.34	274	93.0	45.3	42.8	0.8	14
U9215 O1	...	...	2.0	0.15	329	49.3	11.9	10.0	0.6	14
U9299	9.8	61[1]	0.5	0.09	255	23.0	15.9	3.0	0.4	22

$\Omega_{\rm beam}$: beam area, the physical region sampled by the 115-GHz beam and used to derive the surface densities. i: inclination, used to correct measured values to face-on. $\Sigma_{\rm H_2,CO}$: CO inferred H_2 surface density corrected to face-on. $\Sigma_{\rm d,0}$: dust mass surface density measured in the area of the IRAM ^{12}CO(1 − 0) beam and corrected to face-on. G/D: gas/dust ratio expected from the metallicity according to Draine et al. (2014) and Eqn 6. $\Sigma_{\rm g,0}$: Total face-on H surface density derived from $\Sigma_{\rm d,0}$ and G/D. $\Sigma_{*,0}$: face-on stellar mass surface density averaged in the region of the ^{12}CO(1 − 0) beam using stellar mass maps created from the g and i SDSS images and the Zibetti et al. (2009) stellar mass prescription. $P_{\rm ext}/k$: mid-plane hydrostatic pressure using equation (5). $f_{\rm H_2,th}$: molecular fraction $M_{\rm H_2}/(M_{H\,1} + M_{\rm H_2})$ from equation (4). The final column is the ratio of $f_{\rm H2}$ estimated theoretically based on the dust density and equation (4) and that estimated directly from the CO measurements. References: [1]LEDA[19] (Makarov et al. 2014); [2]Guthrie (1992).

$L'_{21}/L'_{10} = T_{\rm B}^{21}/T_{\rm B}^{10} = I_{21}/I_{10}$. The 22 arcsec beam of IRAM at 115 GHz probes a physical scale of 2–3 kpc at the distance of these sources, meaning that we cannot assume either a point source or a uniformly extended source geometry. In order to interpret our line ratios measured with different beams (^{12}CO(1 − 0) = 21.5″ , , ^{12}CO(3 − 2) = 17.5″ , , ^{12}CO(2 − 1) = 10.7″), we have to make corrections based on assumptions about how the gas is distributed.

There are various ways in which corrections for mismatched beams are attempted in the literature (e.g. Braine & Combes 1992; Cormier et al. 2014; Grossi et al. 2016; Hunt et al. 2017). Following Hunt et al. (2017), we used the 160- μm maps from our *Herschel* PACS imaging to make a direct estimate of the relative surface brightness of 160 μm emission within 22 , 18 , and 11 arcsec beam sized regions at the locations of our pointings. This assumes that the CO distribution will follow that at 160μm. Using this method gives correction factors of 0.64–1.09[9] for R_{21} and 0.82–1.08 for R_{31}, which are listed in Table 3.[10]

The distributions of our corrected R_{21} and R_{31} values compared to the literature are shown in Fig. 3. The R_{21} ratios of BADGRS are consistent with other local samples of spirals and dwarf galaxies, lying in the range 0.6–2.1. This represents a variety of conditions:

(i) *Low excitation* ($R_{21} = 0.4-0.6$): Found in quiescent inter-arm regions of external galaxies and the outskirts of Giant Molecular Clouds (GMCs) and dark clouds (Sakamoto et al. 1995, 1997; Koda et al. 2012; Nishimura et al. 2015). Low ratios can be produced by low-density gas or cold gas with $T_{\rm k} < 10$ K.

(ii) *Normal star forming* ($R_{21} = 0.7-1.0$): Found in the centres of giant molecular clouds and typical star-forming regions in nearby galaxies (Braine & Combes 1992; Sakamoto et al. 1994, 1997; Leroy et al. 2009, 2013; Koda et al. 2012; Cormier et al. 2014, 2016).

(iii) *High excitation* ($R_{21} \geq 1$): Seen rarely in regions such as the Galactic centre (Sawada et al. 2001) and some star-bursting galaxies (Braine & Combes 1992; Hunt et al. 2017). To excite the gas to $R_{21} > 1$ the conditions could be warm, dense and optically thin with $\tau_{21} < 5$ (Sakamoto et al. 1997). It is also possible to have such high ratios if the gas is in optically thick dense clumps and heated externally by a strong radiation field.

The errors on the high $R_{21} > 1$ ratios in NGC 5496 O1,O2 and UGC 9299 are large enough that they are still consistent with a 'normal' $R_{21} = 0.7-1.0$ value, however UGC 9215 O1 appears to be significantly excited with $R_{21} = 2.11 \pm 0.58$.

The R_{31} ratios in Fig. 3(b) are on average lower than the samples of Mao et al. (2010) and Hunt et al. (2017). The lowest ratios ($0.2 < R_{31} < 0.3$) are in the outer disc regions (O2) of the two most massive galaxies, NGC 5584 and NGC 5496. At face value this low ratio indicates very cold (∼10−20K) and/or low density ($n \sim 1000 - 2000\,{\rm cm}^{-3}$) clouds similar to those found in the quiescent disc regions of external galaxies (Wilson et al. 2009; Zhu et al. 2009), however, the R_{21} values at these locations are relatively high. The spectra in Fig. 2 show that in these regions $\Delta v_{32} < \Delta v_{10}$, which indicates that the warm, dense gas is located in more compact regions than the cooler, more diffuse gas that dominates the J = 1–0 emission. We believe that it is this different filling factor for the two transitions which leads to a low beam averaged R_{31}. This is especially evident in the NGC 5496 O2 region, where the ^{12}CO(3 − 2) line is very much narrower than the ^{12}CO(1 − 0) line. This is a highly inclined galaxy and the large sight-line through the disc exacerbates this effect. The regions with the highest R_{21} and R_{31} are those in the outer disc of UGC 9215 and in UGC 9299. That the R_{31} ratios are also high (and less prone to uncertainty due to the closer match of the beam areas), supports the earlier conclusion of more excited, dense gas typical of star-forming regions. The centre of UGC 9215 has an intermediate value of $R_{31} \sim 0.53$ while for UGC 9215 O1 and UGC 9299 the ratio is $R_{31} > 0.70$, which is more typical of star-bursts, luminous infrared galaxies (LIRGs),

[9]The correction can be greater than unity because a larger beam placed at the edge of an exponential distribution will see a higher surface brightness than a smaller beam, as the large beam samples closer to the peak of the exponential

[10]Instead, if we assume that the molecular gas is distributed as an exponential disc with scale-length ∼0.2R_{25} (Young et al. 1995; Leroy et al. 2009; Kuno et al. 2007) we find slightly smaller but comparable values (0.58–1.03 for R_{21}).

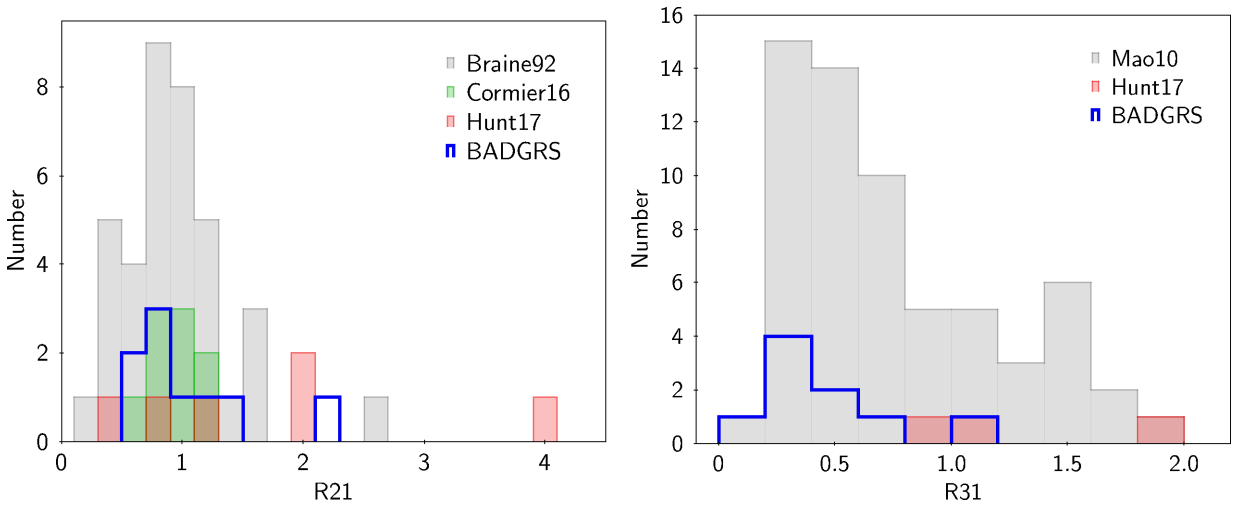

Figure 3. (a) Distribution of R_{21} and (b) R_{31} for BADGRS compared to literature samples of normal spirals from Braine & Combes (1992) and Mao et al. (2010) and low-metallicity galaxies from Hunt et al. (2017). The BADGRS have similar R_{21} ratios as other samples, but are less excited in the R_{31} ratio compared to the low-metallicity galaxies.

and actively star-forming regions where $R_{31} \sim 0.5-0.8$ (Yao et al. 2003; Narayanan et al. 2005; Mao et al. 2010; Papadopoulos et al. 2012; Bauermeister et al. 2013). We find no trend for the R_{31} ratio to be higher in the centre of these galaxies compared to further out in the disc.

The isotopologue ^{12}CO/^{13}CO ratio R_{10} is useful for breaking degeneracies in the low excitation CO spectral line energy distribution (SLED; e.g. Papadopoulos et al. 2012). We present measurements or upper limits for the ratio R_{10} in Table 3, using the ^{12}CO(1 − 0) line-widths given in Table 2. Low values of $R_{10} = 5-10$ indicate a cold, quiescent phase with high ^{12}CO optical depth whereas higher values of $R_{10} \geq 15$ favour lower optical depth, vigorous star formation with turbulent and diffuse clouds. We detect ^{13}CO(1–0) only in the centre of NGC 5496 where we see clear signs of a cold, high optical depth, and quiescent molecular ISM with $R_{10} = 4.2 \pm 1.1$. In NGC 5584, the lower limit of $R_{10} > 13$ suggests that the gas in this galaxy may have lower optical depth or a lower ^{13}C abundance. For the other positions there are no useful limits on R_{10}.

4 DUST AND MOLECULAR GAS PROPERTIES

Dust emission usually shows a strong correlation with CO emission, and by inference, H_2 content (Young et al. 1995; Dunne et al. 2000; Dunne & Eales 2001; Corbelli et al. 2012; Foyle et al. 2012; Scoville et al. 2014; Grossi et al. 2016; Hughes et al. 2017). This relationship has been exploited by many studies at both high and low redshift which use dust as an alternative tracer for molecular gas. The applications range from resolved studies in the Milky Way and nearby galaxies, where dust emission is used in combination with H I and CO to derive α_{CO} factors or measure total H_2 content (Dame, Hartmann & Thaddeus 2001; Draine et al. 2007; Bot et al. 2010; Gratier et al. 2010; Roman-Duval et al. 2010; Bolatto et al. 2011; Leroy et al. 2011; Smith et al. 2012b; Sandstrom et al. 2013; Shi et al. 2014) to the potential use of dust emission at higher redshift as a substitute for CO altogether (Magdis et al. 2012; Rowlands et al. 2014; Scoville et al. 2014; Genzel et al. 2015; Scoville et al. 2016; Hughes et al. 2017). Given the increasing use of dust as a tracer for gas, it is important to understand if there are instances where that assumption breaks down. In this section, we will compare the dust mass with the molecular gas mass derived from the CO data.

4.1 SED fitting and dust mass estimation

The *Herschel*-ATLAS data are used to estimate the dust properties of the four galaxies, using a two-temperature modified black body to describe the SED. The total fluxes for NGC 5584 and NGC 5496 are taken from De Vis et al. (2017a), while for UGC 9215 and UGC 9299 updated FIR photometry was measured from the maps using manually defined apertures to avoid contamination from background sources. The *Herschel*-SPIRE photometry includes the $K_{col}P$ and K_{beam} corrections[11] (1.019, 1.0019, 1.005 at 250, 350, and 500-μm) and aperture corrections as described in Valiante et al. (2016). For *Herschel* PACS, we did not apply a colour correction as the SED shapes were close to $F_\nu \propto \nu^{-1}$ for the 100 and 160 μm points. We also used the IRAS 60- μm flux in the SED fit and constrained the maximum warm dust contribution by using the *WISE* 22- μm flux as an upper limit. More details of the photometry are in Clark et al. (2015) and De Vis et al. (2017a). We use a value for the dust mass absorption coefficient of $\kappa_{250} = 0.56\,m^2\,kg^{-1}$, which gives masses a factor 1.59 times higher than Clark et al. (2015) and De Vis et al. (2017a) (and for reference 1.4 times *lower* than other commonly adopted opacities from the Draine et al. 2007 model). This updated coefficient is derived from the *Planck* 857-GHz measurement of the dust opacity per H nucleon assuming a dust-to-gas ratio of 1 per cent, and scaling to 250 μm using $\beta = 1.75$ as measured for this part of the spectrum in Planck Collaboration XIX (2011). Of course, wherever we compare dust masses to other samples from the literature we scale all masses to the value of κ_{250} used here.

When well sampled, the dust SED between 60 and 1000μm in star-forming galaxies is not well represented by a single temperature-modified blackbody because the dust is at a range of temperatures (e.g. Devereux & Young 1990; Dunne et al. 2000; Dunne & Eales 2001; Dale & Helou 2002; Draine et al. 2007; Galliano et al. 2011; Clark et al. 2015; Hunt et al. 2015; Rémy-Ruyer et al. 2015). Warm (>30 K) dust is located near to regions of star formation while dust in the diffuse ISM is heated by the interstellar

[11] See section 5 of http://herschel.esac.esa.int/Docs/SPIRE/spire_handbook.pdf

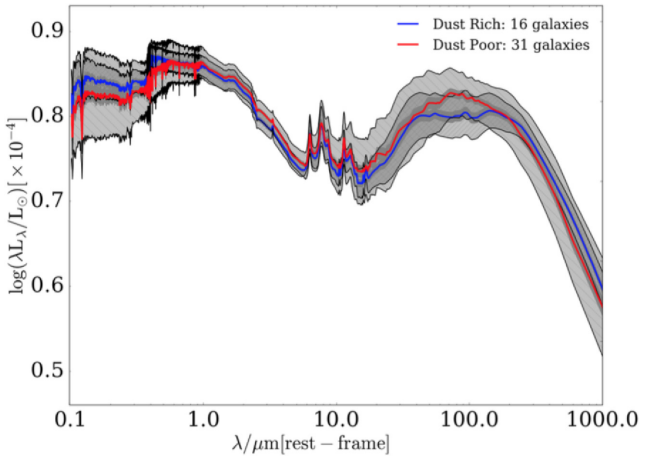

Figure 4. Stacked best-fitting SEDs from MAGPHYS for BADGRS (blue) and non-BADGRS from the sample of Clark et al. (2015). The BADGRS have broad and flat IR SEDs showing significant emission from cold dust. This figure is reproduced from Schofield (2017).

radiation field (ISRF) to cooler temperatures of 10–25 K.[12] While in reality the dust is at a range of temperatures along the line of sight, a reasonable estimate of the dust mass is obtainable by fitting a two temperature component modified blackbody (2MBB), as described in Dunne & Eales (2001). The bulk of the dust mass is contained in the diffuse, colder component and so as long as the SED-fitting method allows this to be separated from the hotter components, we do not miss a large fraction of the dust mass. This method gives similar dust masses to that of Draine et al. (2007), who allow the dust to be heated by a radiation field with a power-law distribution. The errors on the temperatures and dust masses are calculated using the χ^2 distribution for the SED fits for each parameter, and represent the 68 per cent confidence interval. Our two component modified blackbody fits to the 60–500 μm photometry produces parameters very similar to those in Clark et al. (2015), and we repeat their finding that the diffuse dust temperatures for the BADGRS sample are significantly cooler (∼13−15K) than those in more massive spirals and low metallicity dwarf galaxies (18–31K) (Clark et al. 2015; Hunt et al. 2015; Rémy-Ruyer et al. 2015). This is illustrated in Fig. 4 where the stacked best-fitting SEDs from MAGPHYS for BADGRS and non-BADGRS from the samples of Clark et al. (2015) and De Vis et al. (2017a) are compared. The BADGRS dust SED has a much flatter peak and relatively more emission in the sub-millimetre part of the spectrum where the cold dust dominates. A broader FIR SED shape for lower stellar mass, lower metallicity galaxies has been noted before and is thought to be due to a larger range in ISRF intensities across the low attenuation galaxies, allowing dust to be heated to higher temperatures (Ciesla et al. 2014; Cortese et al. 2014; Rémy-Ruyer et al. 2015). However, the ubiquitous very cold diffuse dust temperatures we see in BADGRS have not been found in other samples.

To estimate the dust mass within the same region as the CO emission we use the 250- μm map as it has the closest intrinsic resolution to the CO data without sampling a larger beam area, and is also the highest sensitivity map from *Herschel*. We convolve the 250- μm map to the same resolution as the ^{12}CO(1 − 0) data[13] and use the pixel value at the location of the CO pointing to give S_{250}(CO).[14] The dust mass in the area covered by the IRAM beam at 115 GHz, M_d(CO), is then derived from

$$M_d(\mathrm{CO}) = (S_{250}(\mathrm{CO})/S_{250}(\mathrm{tot})) \times M_d(\mathrm{tot}).$$

This scaling simply assumes that the cool dust SED is similar on these scales within the galaxy. These galaxies do not have large bulges and therefore there is no expectation of a strong radial temperature gradient for the diffuse dust component which dominates the dust mass. We cannot perform the 2MBB fitting to the individual regions, as these galaxies are unresolved by IRAS at 60- μm.

The local dust masses in each CO region are listed in Table 4 and are also compared to the local M_{H2} masses derived from the ^{12}CO(1 − 0) data.

4.2 Molecular gas-to-dust ratios and star formation efficiency

For a metallcitiy-dependent α_{CO}, the M_{H_2}/M_d ratios for BADGRS range from 7 to 27 with a mean $M_{H_2}/M_d = 16$ (the mean using the α_{MW} is 11). This is lower by a factor ∼10 compared to the $M_{H_2}/M_d \sim 100 - 150$ seen in local spirals (Dunne & Eales 2001; Leroy et al. 2011; Sandstrom et al. 2013), as illustrated in Fig. 5 which compares the dust and molecular gas properties for the BADGRS, HRS (Boselli, Cortese & Boquien 2014), and star-forming Virgo dwarfs (Grossi et al. 2016). The dashed lines in Fig. 5(a) represent constant M_{H_2}/M_d ratios of 1000, 100, and 10 (top to bottom). Fig. 5(b) shows that BADGRS display a much lower H_2-per-unit-dust-mass at the same metallicities as other galaxies. There is no obvious trend of M_{H_2}/M_d with metallicity.

To be certain that these low M_{H_2}/M_d ratios are not produced purely by the conversions from observed quantities to dust and H_2 mass, we compare the observed quantities in Fig. 6. There is a tight relationship between CO emission and 250- μm flux in local galaxies from the HRS (Corbelli et al. 2012) and star-forming dwarf galaxies in Virgo (Grossi et al. 2016). Both the massive metal-rich sources from the HRS and the more metal-poor Virgo dwarfs lie on the same $F_{CO}-F_{250}$ relation.[15] The BADGRS are deficient in CO emission at a given 250- μm flux, meaning their anomalously low gas-to-dust ratios are not artefacts of the methods used to convert from flux to mass.

In Fig. 7(a), we show the scaling relation for molecular gas and stellar mass. TheM_{H_2}/M_* ratios for the BADGRS are for the individual pointings; the stellar mass in the area of the IRAM beam is derived from smoothed stellar mass maps created from the *g* and *i* SDSS images and the Zibetti, Charlot & Rix (2009) stellar mass prescription. From the literature, we include the stellar mass-selected COLDGASS (Saintonge et al. 2011; Huang & Kauffmann 2014), ALLSMOG (Bothwell et al. 2014, 2016), and HRS (Boselli et al. 2014) samples and also the star-forming Virgo dwarfs (Grossi et al. 2016). Adjustments have been made to literature values in

[12]Cold dust may also be present in dense starless cores, but this is not thought to dominate the mass of dust, at least in normal galaxies (Draine et al. 2007).

[13]This is a small change as the 250- μm beam is 18.5 arcsec and the^{12}CO(1 − 0) beam is 21.5 arcsec .

[14]The peak pixel flux is corrected by the factor 1/0.95 to account for the effects of pixelization as described in the SPIRE manual.

[15]We followed the same prescription as Grossi et al. (2016) to estimate S_{250} (*beam*), which is to use an aperture of radius 18.5 arcsec . Note this is not the same as our own values given by the convolution of the *Herschel* maps to the same resolution as the IRAM data, the Grossi et al. (2016) method results in higher dust fluxes.

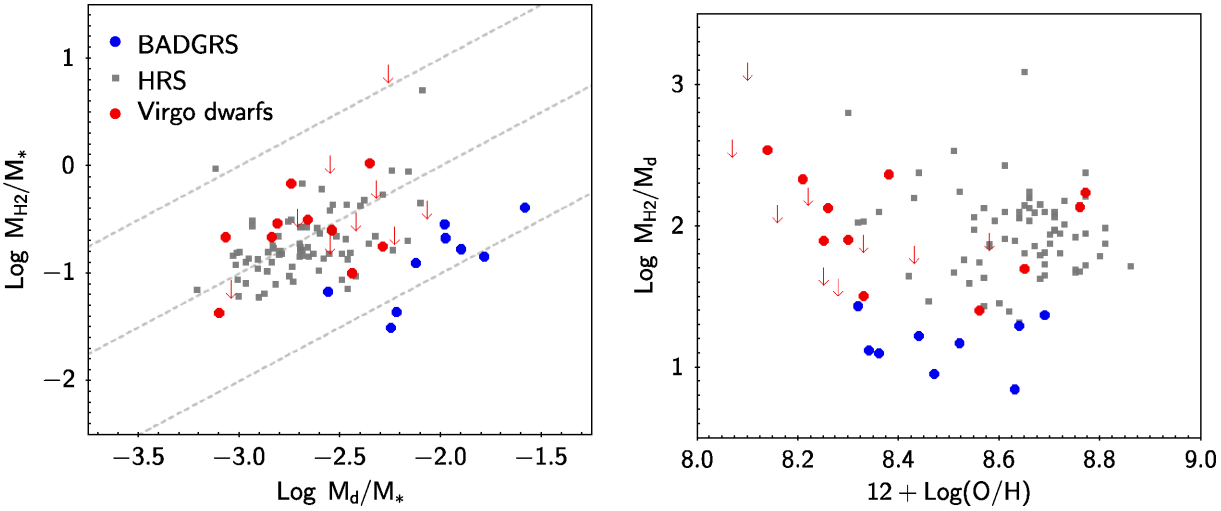

Figure 5. (a) The correlation between dust and molecular gas mass having normalized by the common scaling factor of stellar mass. The dashed lines indicate constant $M_{\rm H_2}/M_{\rm d}$ ratios of 10, 100, and 1000 (bottom to top). BADGRS are the most dust-rich (relative to M_*) galaxies and lie below the extrapolated trend for $M_{\rm H_2}/M_{\rm d}$ from the other samples. (b) Molecular gas to dust ratio as a function of metallicity. There is no correlation, but BADGRS lie clearly below the average $M_{\rm H_2}/M_{\rm d}$ ratios for the other samples. Metallicities are all in the O3N2 calibration of Pettini & Pagel (2004). Dust masses for the HRS are from MAGPHYS (De Vis et al. 2017a), while dust masses for Virgo dwarfs are scaled from the $\beta = 2$ version in Grossi et al. (2016) to be comparable to MAGPHYS as follows. The HRS MAGPHYS dust masses were compared to those determined by Grossi et al. (2016) using their single MBB $\beta = 2$ method. A tight correlation with linear slope, and an offset of $\mathrm{Log}\,(M_{\rm d,MP}/M_{\rm d,G16}) = 0.23$ dex was found (once all were scaled to the same $\kappa_{\rm d}$). This difference is due to MAGPHYS fitting a more realistic temperature distribution which captures better the colder dust component. We scale the Virgo dwarf dust masses up by this amount to be consistent with HRS and BADGRS. All dust masses are scaled to a common $\kappa_{250} = 0.56\,\mathrm{m^2\,kg^{-1}}$.

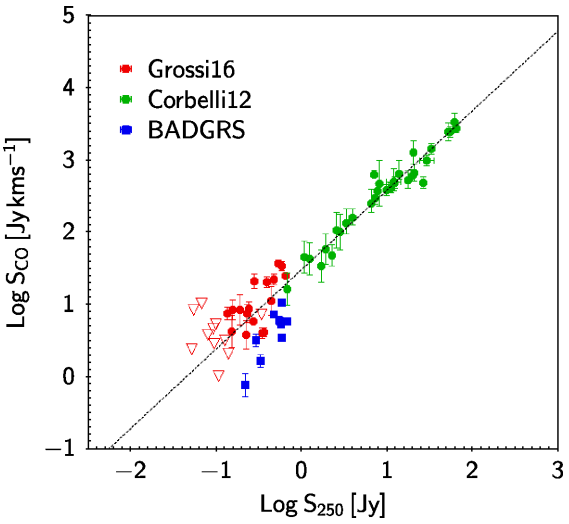

Figure 6. The tight correlation of CO and sub-mm fluxes first presented in Corbelli et al. (2012) and updated in Grossi et al. (2016). We reproduce the literature data here and compare to our BADGRS sample. The open triangles represent upper limits. The dotted line is the best fit from Grossi et al. (2016) to the red and green points. These fluxes are single IRAM CO fluxes in a 22 arcsec beam compared to the 250- μm flux in an aperture with radius 18.5 arcsec as described in Grossi et al. (2016). It can be seen that the BADGRS lie below the relationship found in other samples.

order to bring all measurements onto common scalings, see caption to Fig. 7 for details. We show two locations for the BADGRS: dark blue circles are using the total stellar mass on the *x*-axis, cyan circles are using the stellar mass within the IRAM beam. A better comparison, given our resolved observations, is to use the stellar mass surface density on the abscissa rather than total stellar mass. Fig. 7(b) shows more correctly that there is no difference between the BADGRS $M_{\rm H_2}$-M_* scaling and those of other local samples.

The well-studied correlation of $L_{\rm IR}$ and $L'_{\rm CO}$ for a range of sources at low and high redshift is shown in Fig. 8(a). The relationships for normal star-forming galaxies and 'mergers/starbursts' derived by Genzel et al. (2010) are overplotted as solid and dashed lines, although there is contention in the literature as to whether there really is a separate relationship for starburst mergers and normal galaxies (e.g. Casey et al. 2014; Lee et al. 2017; Villanueva et al. 2017). BADGRS, local ULIRGS, and high-z SMGs have a higher $L_{\rm IR}/L'_{\rm CO}$ on average than normal star-forming galaxies at a range of redshifts. Notably the sources with low CO SNR (open red diamonds) in the VALES sample of 160-μm-selected galaxies (Villanueva et al. 2017) also lie in this region of parameter space. These may either be examples of lower luminosity systems with high dense gas fractions (like SMGs and ULIRGs), or higher luminosity, higher redshift examples of BADGRS.

Fig. 8(b) shows the star formation efficiency (SFR/$M_{\rm H_2}$) (or inverse of the depletion time-scale) as a function of $L_{\rm IR}$ for the same samples. Only low-J ^{12}CO(1 − 0) and ^{12}CO(2 − 1) lines are used to create this plot meaning that we are not affected by uncertainties in CO excitation. For Log $L_{\rm IR} > 11.0$, the SFR is estimated using the $L_{\rm IR}$–SFR relationship of Kennicutt (1998) for a Chabrier (2003) IMF, while for the local samples of less obscured galaxies, a combination of IR, Hα, and UV emission is used to capture the total SFR. For BADGRS, we have used the FUV and IR emission in the CO regions to estimate the local SFR as described in Section 2.1. BADGRS are shown as blue circles using the metallicity-dependent $\alpha_{\rm CO}$ from Table 4, connected to yellow squares for the values using the Milky Way $\alpha_{\rm CO}$. Literature samples have $\alpha_{\rm CO}$ as described in the caption.[16]

[16]There remains an active debate over the most appropriate $\alpha_{\rm CO}$ value to use for higher redshift systems and SMGs, with recent work finding values

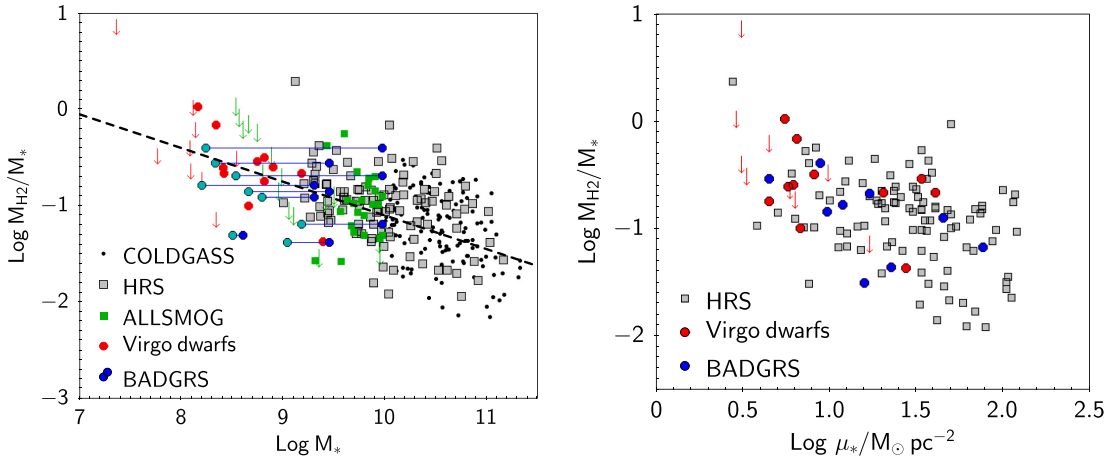

Figure 7. (a) M_*– $M_{\rm H_2}$ scaling relation with the relationship from Bothwell et al. (2014) for the ALLSMOG galaxies shown as black dashed line. All $M_{\rm H_2}$ include He. BADGRS are shown both at their global stellar mass (dark blue circles) connected to the stellar mass in each pointing (cyan circles). When only the local values within the pointing are used (cyan) the BADGRS show a tight relationship but offset to lower $M_{\rm H_2}/M_*$ at similar stellar mass. Using the total stellar mass on the x-axis results in the dark blue points, which are comparable to the other samples of spirals and dwarfs, which are mainly selected based on their stellar masses. Only late type HRS galaxies with a beam filling fraction greater than 10 per cent of the optical area are shown (Boselli et al. 2014), as the uncertainty of the extrapolation to total CO flux becomes too uncertain. The ALLSMOG points use a value of $r_{21} = 0.7$ rather than $r_{21} = 1$ as in Bothwell et al. (2014); this is more typical of the ratio observed in similar samples. The conversion from $L_{\rm CO}$ – $M_{\rm H_2}$ for the BADGRS, Virgo dwarfs, HRS, and ALLSMOG use the (Wolfire et al. 2010) metallicity-dependent $\alpha_{\rm CO}$. The COLDGASS data points are from Huang & Kauffmann (2014), who use a matched 22 arcsec region for stellar mass and $M_{\rm H_2}$, and a constant $\alpha_{\rm CO}$(MW) factor (they only include high stellar mass, high metallicity galaxies). Stellar masses for all the samples are estimated in ways that do not produce any large systematic offsets. (b) $M_{\rm H_2}/M_*$ versus stellar mass surface density for those samples with available data. In this plot there are no differences between the BADGRS and other samples.

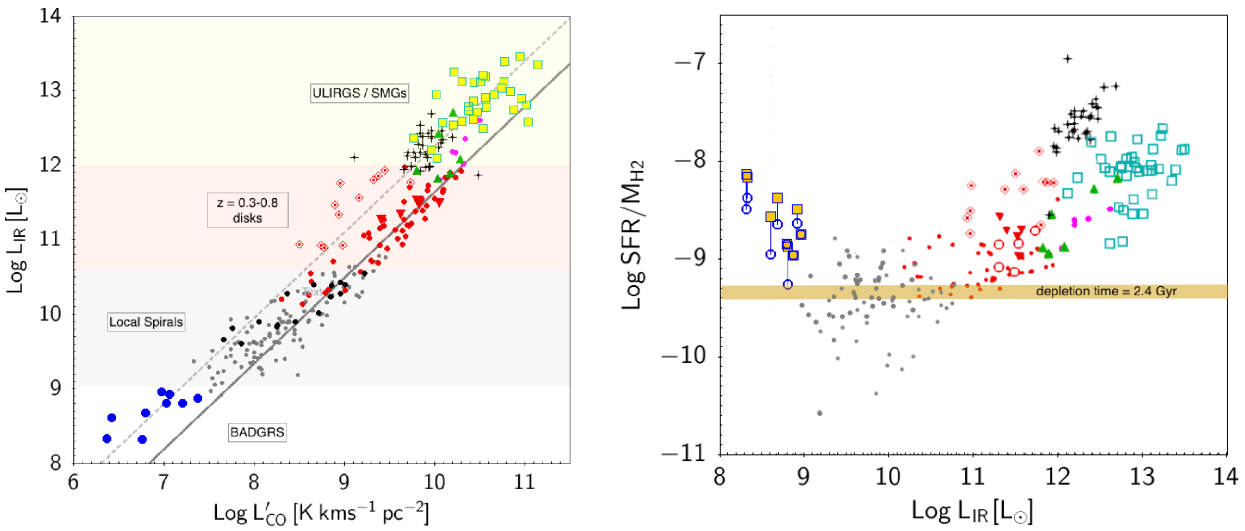

Figure 8. (a) The correlation between $L_{\rm IR}$ and L'_{10} for the BADGRS and other samples from the literature. Only ^{12}CO(1 – 0) or ^{12}CO(2 – 1) measurements are used to avoid uncertainty from excitation corrections. Where ^{12}CO(2 – 1) are used, the conversion used in the literature reference is given below. Grey circles: local spirals from HRS (Boselli et al. 2014), only late-type HRS sources with CO observations covering more than 10 per cent of the optical disc and which have metallicity measurements are shown. Black circles: local discs (Wilson et al. 2009 and $r_{21} = 0.8$ Leroy et al. 2008, 2009); red: intermediate redshift spirals (VALES $z = 0.1 - 0.3$; Villanueva et al. 2017, diamonds: low SNR CO detections), red triangles: $z \sim 0.4$ discs (Geach et al. 2011); black crosses: local ULIRGs (Solomon et al. 1997); green triangles: $z = 0.3$–0.8 250- μm-selected ULIRGs ($r_{21} = 0.75$; Magdis et al. 2014); magenta: BzK ($r_{21} = 0.84$ Daddi et al. 2010); yellow squares: SMG (Ivison et al. 2011; Aravena et al. 2016, $r_{21} = 0.8$, Frayer et al. 2008). The dotted and solid lines are the relationships derived by Genzel et al. (2010) for mergers and normal galaxies, respectively. (b) Star formation efficiency (SFR/ $M_{\rm H_2}$) as a function of $L_{\rm IR}$ using $\alpha_{\rm CO} = 0.8$ for local ULIRGs (Solomon et al. 1997; Downes & Solomon 1998), $\alpha_{\rm CO}$(Z) from Wolfire et al. (2010) for the HRS, and $\alpha_{\rm CO}$ as derived by the authors for the SMG from Ivison et al. (2011). All other points use $\alpha_{\rm CO} = 4.3$. For BADGRS, we use $\alpha_{\rm CO}$(Z) from Table 4 (blue open circles) connected to the values using $\alpha_{\rm CO} = 4.3$ (yellow). The brown-shaded region is the average $\tau_{\rm dep}$ found for local spiral discs by Schruba et al. (2011) and Bigiel et al. (2011).

There is a broad correlation, with the most luminous IR systems having a higher star formation efficiency (or shorter depletion time-scale). Fig. 8(b) implies that BADGRS have higher star formation efficiencies (shorter depletion time-scales) than other local galaxies, and in fact have star formation efficiencies similar to intermediate redshift LIRGS and ULIRGS. There is building evidence that local low mass, low-metallicity galaxies really do have shorter depletion time-scales (Saintonge et al. 2011; Bothwell et al. 2014; Huang & Kauffmann 2014; Hunt et al. 2015; Amorín et al. 2016; Bothwell et al. 2016). Such findings were previously dismissed as the result of not correcting α_{CO} for the effects of metallicity variations (Leroy et al. 2011), but later studies which are able to make these corrections still find the same trends.

5 A MOST UNUSUAL MOLECULAR ISM IN BADGRS

While BADGRS are very rich in atomic gas and dust, they are inexplicably deficient in CO, our single dish observations revealing weak, narrow CO lines with an intensity far lower than that expected from their dust emission. It is important to understand the reasons for this, given that the use of both CO and dust (e.g. Genzel et al. 2015; Scoville et al. 2017) to estimate molecular gas masses is commonplace at high redshift. If either tracer can depart from its usual relationship in a class of galaxy, then clearly it would lead to systematic biases in the estimation of ρ_{H_2} and its evolution.

We now consider some possible explanations for the unusual dust-H_2 or dust-CO ratios. In Section 5.1, we look at the possibility that conditions for H_2 are unfavourable and the ISM is simply H I dominated. In Section 5.2, we investigate whether the CO is adequately shielded from photodissociation by measuring the dust attenuation in the sources in a variety of ways. In Section 5.3, we return to the observation that BADGRS have very cold diffuse dust temperatures and discuss the implications for the dust properties and geometry, which may have a bearing on the dust to CO ratio. In Section 5.4, we highlight recent work which suggests that cosmic rays may be a culprit for destroying CO throughout the volume of a clouds and finally in Section 5.5, we look at evidence for a bursty star formation history in BADGRS and speculate on how that might affect the relative abundance of dust and CO.

5.1 Unfavourable conditions for formation of H_2

If conditions in the ISM of BADGRS do not favour the formation of H_2, they may be H I dominated and the dust simply traces the atomic component. This is often the case in low metallicity, diffuse dwarf galaxies (which also have low dust content). The formation of H_2 requires certain combinations of column density, pressure and radiation field (e.g. Elmegreen 1993; Papadopoulos, Thi & Viti 2002) and the relationship between the hydrostatic mid-plane pressure and the molecular fraction (Blitz & Rosolowsky 2006; Leroy et al. 2008; Bekki 2014; Valdivia et al. 2016) has a functional form in gas-rich galaxies (Feldmann et al. 2012):

$$R_{\rm mol} = \Sigma_{H_2}/\Sigma_{H\,I} = \left(\frac{P_{\rm ext}/k}{P_0/k}\right)^{0.7-1.3} \quad (4)$$

where the exponent depends on whether the galaxy is in the H_2 or H I-dominated regime.[17] This is related to the molecular fraction per unit gas mass as $f_{H_2} = (1 + 1/R_{\rm mol})^{-1}$.

The hydrostatic mid-plane pressure for a disc that can be dominated by gas rather than stars (as is the case here) is given by Elmegreen (1989) and Swinbank et al. (2011):

$$\frac{P_{\rm ext}}{k} = 33.3 \times \Sigma_g \left[\Sigma_g + \left(\frac{\sigma_g}{\sigma_*}\right)\Sigma_*\right], \quad (5)$$

where Σ_g/Σ_* are the gas/stellar surface densities in units of $M_\odot\,pc^{-2}$, and σ_g and σ_* are the gas and stellar velocity dispersions. While we do not yet have the high resolution H I data to hand to directly measure $\Sigma_{H\,I}$ over the same area as the dust and CO measurements, we can make a rough estimate of the total gas mass surface density, $\Sigma_g = \Sigma_{H\,I} + \Sigma_{H_2}$, using the measured dust mass surface density and the relation from Draine et al. (2014):

$$\Sigma_{g,0} = (0.0065\,Z/Z_\odot)^{-1}\,\Sigma_d \times \cos i, \quad (6)$$

where we have reduced the constant in the Draine et al. (2014) equation by a factor 1.4 to be consistent with the value of dust opacity we are using (Planck Collaboration XIX 2011).

$\Sigma_{*,0}$ is the face-on stellar mass surface density averaged over the $^{12}CO(1-0)$ beam using smoothed stellar mass maps created from the *g* and *i* SDSS images and the Zibetti et al. (2009) stellar mass prescription. The dust, gas, and stellar surface densities are listed in Table 5.

We do not yet have direct measures of the stellar and gas velocity dispersions (σ_g/σ_*) although in future they will be obtained from higher resolution H I data and optical IFU data. For simplicity, the pressure calculation will assume that $\sigma_g/\sigma_* \sim 1$ as is found for dwarfs in O'Brien, Freeman & van der Kruit (2010). Alternatively, taking a likely gas velocity dispersion within r_{25} of $\sigma_g = 15\,km\,s^{-1}$ Tamburro et al. (2009) and $\sigma_* \sim 25\,km\,s^{-1}$ based on measurements from Martinsson et al. (2013), and using $V_{rot}/\sigma \sim 0.2$ for late type low mass galaxies does not affect the conclusions.[18]

The pressures we estimate in 2–3kpc regions using the above assumptions are in the range $P_{ext}/k \sim 1 - 40 \times 10^4\,K\,cm^{-3}$. At these pressures we expect $\Sigma_{H_2} \geq \Sigma_{H\,I}$ at 7/9 locations, the exceptions being the outer disc of NGC 5496 and UGC 9299. In the final column of Table 5, we compare the molecular fraction derived using the arguments just described ($f_{H_2,th}$), to that estimated directly from CO using the metallicity-dependent $\alpha_{CO}(Z)$:

$$f_{H_2,CO} = \Sigma_{H_2,CO}/\Sigma_g.$$

The surface density of molecular gas as traced by CO is a factor 3–22 (mean 11) times lower than expected given the dust emission, metallicity, and stellar mass surface density measured in each region.

Resolved studies of nearby spirals and dwarfs (Bigiel et al. 2008; Leroy et al. 2008) find a marked transition from H I–H_2 with equal contributions occurring at a gas mass surface density of $\sim 10\,M_\odot pc^{-2}$. Our dust-based Σ_g estimates in Table 5 are all at or above this value, although the transition threshold will increase with decreasing metallicity.

In summary, it appears that lack of favourable conditions for formation of H_2 in the ISM of these galaxies is not the culprit, but

intermediate between the ULIRG and Milky Way values (Weiß et al. 2005; Ivison et al. 2011; Bothwell et al. 2017; Carleton et al. 2017) but see also Aravena et al. (2016). If we instead used the $\alpha_{CO} = 0.8$ ULIRG value for the SMGs at high redshift, this shifts the open cyan squares up to lie closer to the ULIRGS but it does not affect the discussion related to the BADGRS.

[17] The normalization and slope of the $R_{\rm mol} - P_{\rm ext}$ relation in Feldmann et al. (2012) were found to scale with metallicity and we have included this scaling in our determination of $R_{\rm mol}$ by using the appropriate slope and normalization from their Fig. 3.

[18] V_{rot} is estimated from the H I line-widths and corrected for inclination.

this assumes that the dust is a reliable tracer of the total gas, modulo a metallicity dependence. A future analysis of high resolution H I imaging will allow us to more fully examine the balance between dust, atomic and molecular gas within the discs, and star-forming regions of these sources.

5.2 Photodissociation of CO due to lack of shielding

The usual reason that the ability of CO to trace H_2 breaks down is a lack of shielding for the fragile CO molecule from UV photodissociation (e.g. Lee et al. 2015). When the metallicity (or dust/gas ratio) is low, the region of a molecular cloud at which A_v is high enough to shield the CO is very much reduced (Papadopoulos & Pelupessy 2010; Wolfire et al. 2010; Glover & Mac Low 2011). This in turn means that the CO is only present in the very central cores of the dense clouds, and can be missing from the cloud envelopes or from the entirety of less dense clouds. However, at the metallicities of the BADGRS ($0.5 - 1\,Z_{\odot}$) CO is believed to trace H_2 to within a factor of 2 of the Milky Way α_{CO} scaling (Bolatto et al. 2013). Below these metallicities, CO is efficiently photodissociated leading to regions of 'CO dark' molecular gas where α_{CO} can be 10–100times larger than the Milky Way value (Wolfire et al. 2010). Evidence for CO dark gas has been found in low-metallicity dwarf galaxies (e.g. Leroy et al. 2011; Shi et al. 2014), and in low A_v regions of the Milky Way (Planck Collaboration XIX 2011). A simple comparison of the M_{H_2}/M_d ratios for BADGRS (7–27) with those expected for galaxies of similar metallicity (100–150; e.g. Fig 5) would suggest that 70–90 per cent of the molecular gas in the BADGRS is 'CO dark' and not recovered even with a metallicity-dependent α_{CO}.

Given that these sources were selected on the basis of their dust emission in a volume-limited survey, it would be rather surprising for them to be devoid of CO due to a lack of dust shielding. Estimates of A_{FUV} for HAPLESS, HIGH, and the HRS were made by De Vis et al. (2017a) using the ratio of the attenuated and intrinsic FUV luminosities from MAGPHYS fitting.[19] Interestingly, BADGRS have much lower attenuation ($A_{FUV} \sim 0.2 - 0.8$) than normal spirals ($A_{FUV} = 1 - 3$), even at the same dust mass.

Why do these galaxies have such low attenuation despite their dust and metal content being relatively high? That a given quantity of dust can produce differing amounts of attenuation is directly a question of dust geometry and/or grain properties which affect the attenuation curve. Changes in these may lower the effective shielding for CO at a given metallicity (or dust/gas ratio).

The infrared/UV luminosity ratio, IRX, is a calorific measure of the UV attenuation which is insensitive to geometry (though it does require knowledge of how much dust is heated by UV versus optical photons, Cortese et al. 2008; Viaene et al. 2016). The relationship between IRX and UV slope (β) usefully *is* affected by the dust attenuation curve (which is a combination of star/dust geometry and intrinsic dust absorption and scattering properties), for more details see e.g. Gordon et al. (2000), Kong et al. (2004), Boquien et al. (2009), Buat et al. (2012), Mao, Kong & Lin (2014), Battisti, Calzetti & Chary (2016), Faisst et al. (2017). The UV slope is also sensitive to the age of the stellar population which dominates the UV light, and with complex star formation histories there are many degeneracies, (e.g. Kong et al. 2004; Boquien et al. 2012; Mao et al. 2012).

[19]This is consistent with the A_{FUV} we would derive using the empirical relationship from Cortese et al. (2008) for a similar range of Hubble types, and to the relationship between IRX and A_{FUV} from Hao et al. (2011).

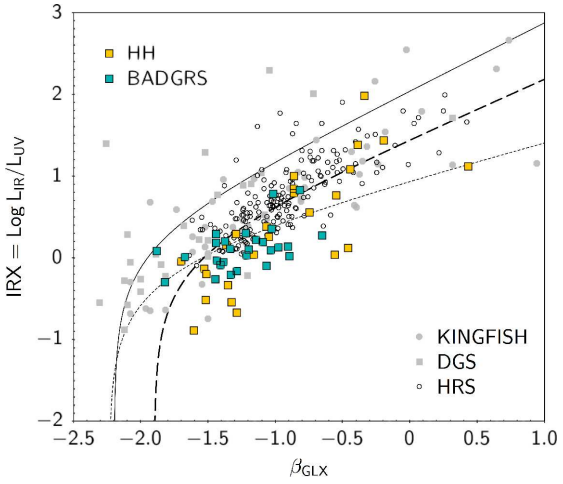

Figure 9. IRX-β for star-forming galaxies in the HRS, KINGFISH, and DGS samples (grey and black points; Skibba et al. 2011; Madden et al. 2013; Ciesla et al. 2014; De Vis 2016; Faisst et al. 2017). Star-forming galaxies from the dust (HAPLESS) and H I (HIGH) selected samples are shown as coloured squares. Those designated as BADGRS based on FUV-K colour and dust/stellar mass ratio are blue while those which are redder and/or more dust poor are gold. Attenuation curves for local starbursts (Overzier et al. 2011), normal galaxies (Takeuchi et al. 2012), and the SMC (Bouwens et al. 2016) are shown as solid, dashed, and dotted lines, respectively. The BADGRS lie offset in the IRX-β space compared with the other samples (including the DGS), which tend to have bluer UV colours at the same attenuation. However so also do many of the H I-selected HIGH sample of De Vis et al. (2017a).

The IRX-β relation for galaxies with type later than S0 and Log sSFR > -11.0 from the combined HAPLESS and HIGH (HH), HRS, KINGFISH, and DGS samples is shown in Fig. 9. These samples have good quality *Herschel* data meaning that L_{IR} is well determined (earlier studies have often relied on templates to infer L_{IR} from data on the short wavelength side of the dust SED which makes them less reliable to compare to). Also shown are the relations for (solid) starbursts (Overzier et al. 2011), (dashed) normal star-forming galaxies (Takeuchi et al. 2012) and (dotted) the SMC (Bouwens et al. 2016), which has a steeper extinction curve. Most of the BADGRS lie on or below the SMC dust curve, having lower UV attenuation at the same UV colour (or redder UV colours at the same UV attenuation). To summarize the differences, the average fraction of HRS, KINGFISH, and DGS galaxies lying below all three attenuation curves is 15, 15, and 3 per cent, respectively. For the combined HAPLESS and HIGH samples the fraction is 63 per cent, while 74 per cent of BADGRS lie below the SMC curve.

Several papers have claimed that high redshift ($z > 5$) galaxies lie below the typical starburst and spiral relations using the Calzetti dust law (Siana et al. 2009; Reddy et al. 2010; Bouwens et al. 2016; Faisst et al. 2017). A more detailed investigation into the IRX-β relationship for the BADGRS (and HAPLESS and HIGH in general) will be presented elsewhere (Dunne et al. in preparation), where we will explore how much of the offset can be ascribed to dust properties and how much to differences in star formation history, and investigate the possibility of using BADGRS as low redshift ISM analogues for high redshift sources.

5.3 Dust emissivity and/or geometry effects

One of the other unusual aspects of the BADGRS ISM is that the dust in the diffuse ISM is much colder (12–16 K) than in spirals or low-metallicity dwarfs (∼18−31K; Clark et al. 2015; Hunt et al. 2015; Rémy-Ruyer et al. 2015). The temperature of dust grains in thermal equilibrium with the interstellar radiation field can be written as

$$T_{\rm d}^{4+\beta} \propto 4\pi \int_{0.09}^{3\mu m} J_\lambda \sigma_\lambda {\rm d}\lambda,$$

where $4\pi J_*$ is the integrated intensity of the radiation field, σ_λ is the dust absorption cross section (which is a function of wavelength), and β is the dust emissivity index. For similar dust properties (i.e. similar σ_λ), such a temperature difference would require an ISRF 20−120× lower in BADGRS than that in spirals and low-metallicity dwarfs. Using the relationship between ISRF and dust temperature from Hunt et al. (2015) [which is based on the Draine et al. (2007) model opacities], we estimate that the BADGRS should have a $U_{\rm min}$ (the radiation field heating the bulk of the dust mass) of ∼0.05−0.1times the local solar neighbourhood ISRF, a factor 10–20 lower than the KINGFISH average (Hunt et al. 2015). While BADGRS have low stellar mass surface densities, their extreme blue SED means that their FUV surface brightness is much higher than typical spirals. By integrating the UV-optical SED fitted with MAGPHYS by De Vis et al. (2017a) and dividing by the area of the aperture used to measure the emission, we can directly measure the bolometric surface brightness of radiation finding values of $\chi = 1.7 - 2.3 \times 10^{-5}\,{\rm W\,m^{-2}}$ (not corrected for internal extinction). These values are similar to the local solar neighbourhood ISRF of $\chi_\odot = 2.2 \times 10^{-5}\,{\rm W\,m^{-2}}$ determined by Mathis, Mezger & Panagia (1983). Thus, the global averaged radiation field is not compatible with the equilibrium dust temperature for dust emissivities similar to those used by Draine et al. (2007), or for dust in the Milky Way.

Possible solutions to this conundrum could be (a) the dust is mainly in dense clumps which are shielded from the ISRF, while remaining optically thin to FIR/sub-mm emission, or (b) the dust is less efficient at absorbing in the UV/optical and/or more efficient at radiating in the FIR/sub-mm. This would translate into a dust absorption coefficient, σ_λ, a factor ∼10−20 different (lower in the UV/optical or higher in the sub-mm) in BADGRS than in the Milky Way and other nearby spirals. Either scenario would allow the dust to remain at a low temperature despite the UV radiation fields, since in case (a) most of the dust does not see the UV photons and in Case (b) the dust does not absorb them as easily; both also naturally explain the low UV attenuation.

The *Planck* mission found cold clumps in the Milky Way with $T_{\rm d}$ ∼13 K and an average density of $2 \times 10^3\,{\rm cm^{-3}}$ (Planck Collaboration XXII 2011; Juvela et al. 2018). If the dust in BADGRS were located in similarly dense clumps then one might expect prolific CO emission since clearly the clumps are well shielded from the UV field. However, CO also freezes out onto dust grains in such conditions (Fontani et al. 2012) and this may well account for a reduction in the CO emission relative to that at sub-mm wavelengths. A geometrical explanation such as this could be investigated using radiative transfer methods, we defer this to a future paper.

If, on the other hand, the dust opacity were different by a factor 10–20, the lack of CO can then be explained by the lack of shielding provided by the dust. If the dust is a much poorer absorber then the UV photons can penetrate deeper into the molecular clouds and destroy the CO, while alternatively if the dust is a more efficient emitter in the sub-mm, we will have overestimated the mass of dust using the Milky Way sub-mm opacity κ_{250}. The dust opacity is determined by the composition and structure of the grains, so such a dramatic change in dust properties across an entire galaxy would be extremely unusual and difficult to explain. The emissivity of dust at sub-mm wavelengths has been observed (Bot et al. 2009; Planck Collaboration XIX 2011; Martin et al. 2012; Planck Collaboration XI 2014; Fanciullo et al. 2015; Ysard et al. 2015; Planck Collaboration XXIX 2016), to increase by a factor ∼2 in dense environments within the Milky Way and varies within the diffuse ISM by smaller factors. It is known that the conditions in dense clouds can lead to changes in the grain structure via aggregation and the formation of ice mantles (Köhler et al. 2012) but such mechanisms do not have time to operate in the diffuse ISM. Instead it is proposed that some other processing, such as FUV irradiation and changes in mantle composition and thickness in the Jones et al. (2013) dust model, as investigated by Ysard et al. (2015) and Fanciullo et al. (2015), can serve to produce (at least qualitatively) the changes measured in the dust SED of the high latitude Milky Way by Planck Collaboration XXIX (2016). It must be noted though that the changes in opacity required in the Milky Way are only of order 20 per cent (40–50 per cent for the extremes). To explain the dust temperatures and CO emission in BADGRS, we would need to invoke far more radical changes.

We defer further investigation of dust properties and geometry for when we have higher resolution sub-mm data and optical measures of attenuation across the galaxies from IFU data.

5.4 Depletion of CO by cosmic rays

Cosmic rays from recent star formation can dissociate CO throughout the volume of a molecular cloud, not just at its surface as is the case in photo-dissocation regions (PDRs). Bisbas, Papadopoulos & Viti (2015) and Bisbas et al. (2017) show that for certain conditions of gas density and cosmic ray ionization rate ($\zeta_{\rm CR}$), CO may be almost completely destroyed rendering only the densest parts of the clouds visible. The effect of cosmic rays are not confined to extreme star formation environments, and even at $\zeta_{\rm CR}$ of 10 times the MW value, there is a marked effect on the CO abundance relative to H_2. Clouds that are low density are more susceptible, so if the molecular clouds in BADGRS were more diffuse than typical GMCs (e.g. $n_{\rm H_2} \sim 100 - 250{\rm cm^{-3}}$), they could become CO depleted even at $\zeta_{\rm CR} \sim \zeta_{\rm MW}$. This would necessitate a population of diffuse, high column density H_2 clouds, which may not be gravitationally bound. A more detailed study will be possible with high-resolution synchrotron data, which will reveal the local $\zeta_{\rm CR}$ across the galaxies, and ALMA data to determine the properties of the molecular gas via high-resolution CO and dust observations.

5.5 Temporary changes in the CO/dust ratio

A range of evidence indicates that many BADGRS are undergoing, or have recently experienced, bursts of star formation.[20] Their UV colours (uncorrected for attenuation) indicate a time-scale of $t_{\rm burst}$ < 300 Myr (Bianchi et al. 2005), while an exploration of the star formation histories from MAGPHYS indicates a higher probability of a burst in the last few hundred Myr for BADGRS compared to HRS.

[20]Not to be confused with a 'starburst' classification based on a threshold in the strength of the current SF relative to past SF. Here, we simply mean an increase in the recent SF rate compared to the past average

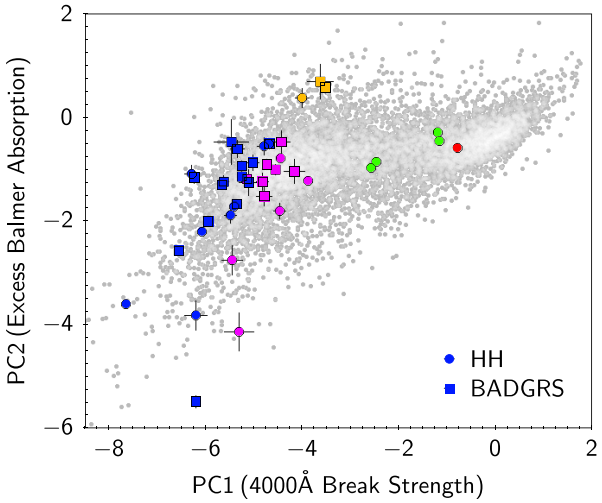

Figure 10. The spectral diagnostic of star-formation history from Wild et al. (2007) showing the location of BADGRS and non-BADGRS within the combined HAPLESS and HIGH samples (HH). The background points are those GAMA galaxies with good-quality spectra in the range $0.05 < z < 0.11$ and $\log M_* > 9.0$. The colours of the points indicate their spectral classifications: blue (starbursts), purple (star forming), yellow (post-starburst), green (green valley), red (quiescent). The spectra support the broad-band SED results from MAGPHYS indicating that most BADGRS are currently or have recently experienced bursts of star formation. The four pilot galaxies are all in the starburst category.

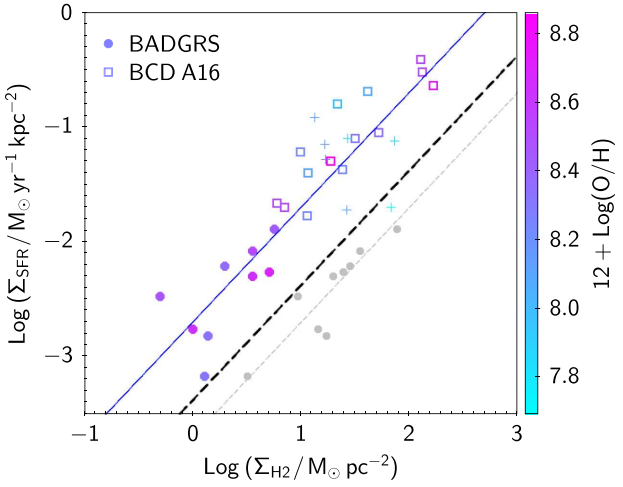

Figure 11. SFR surface density versus molecular gas surface density for the BADGRS (solid circles) and BCD galaxies from Amorín et al. (2016) (open squares, with crosses as upper limits in Σ_{H2}). Both BADGRS and BCD samples use similar methods to correct α_{CO} for metallicity. Metallicity is shown as a colour scale, revealing that the BCD non-detections are the lowest metallicity sources. BADGRS are more diffuse objects than BCD, but have similarly short molecular depletion time-scales compared to samples of local spiral galaxies ($\tau_{dep} \sim 2.4$ Gyr; thick black dashed line). The dust-based Σ_{H_2} estimates for BADGRS (as described in the text) are the grey circles which lie closer to the average values found for more massive, lower sSFR discs. Depletion time-scales of 0.5 Gyr (purple) and 4 Gyr (grey dashed) are also shown for reference.

The optical spectra of the BADGRS show strong emission lines and a small 4000 Å break consistent with ongoing star formation. A classification of the optical spectra of the combined dust and HI-selected samples (HH) based on a Principle Component analysis of the stellar continuum in the 4000 Å break region is shown in Fig.10 (following Wild et al. 2007). BADGRS reside mostly in, or on the border of, the starburst region in Fig. 10, with 70 per cent either currently or having recently experienced a starburst (compared to 47 per cent of the non-BADGR members of the HH sample). The underlying density of points are from the optically selected GAMA survey (Hopkins et al. 2013) and show the typical bimodality of optically selected samples. This illustrates how rare the starburst and post-starbursts are in a typical optical sample, in contrast to their prevalence in our ISM-selected samples.

As noted in Fig. 8(b), the BADGRS appear to have higher SFE (SFR/M_{H_2}) than local spirals. This may also be an indication of a more bursty star formation mode. Fig. 11 shows the surface densities of SFR and molecular gas for BADGRS and a sample of Blue Compact Dwarf (BCD) galaxies from Amorín et al. (2016), who use a very similar metallicity-dependent α_{CO}. This is the Kennicutt–Schmidt (K–S) relation (Schmidt 1959; Kennicutt 1998), where $\Sigma_{SFR} = A \times (\Sigma_{H_2})^N$. For the BADGRS, we use $\Sigma_{SFR_{(UV+IR)}}$ and $\Sigma_{H_2,CO}$ derived from the FUV images, FIR images, and CO measurements using $\alpha_{CO}(Z)$ (Table 5). Both the BADGRS and BCDs have higher SFR per unit H_2 surface density compared to the relations for local spiral discs (black dashed line) which show a constant depletion time-scale of $\tau_{dep} \sim 2.4$ Gyr (Bigiel et al. 2008, 2011; Leroy et al. 2011, 2013; Schruba et al. 2011).[21] The BADGRS are generally higher metallicity than most of the BCDs, and although they have lower surface densities of both SFR and molecular gas (i.e. they are more diffuse galaxies), they have a similar star formation law when we derive Σ_{H_2} from I_{CO}. BCDs are examples of galaxies undergoing significant bursts of star formation, hence their high SFE is thought to be related to this mode of star formation.

As the tendency to have a recent burst seems prevalent in BADGRS we hypothesize that a temporary increase in the dust-to-CO (or dust-to-H_2) ratio may occur following a burst of star formation. The mechanism for this may include rapid dust formation in supernovae (Dunne et al. 2009, 2003; Matsuura et al. 2011; Gomez et al. 2012; Gall et al. 2014; Indebetouw et al. 2014; De Looze et al. 2017) and possible temporary depletion of the local H_2 reservoir and dispersal of molecular clouds by turbulence. For very recent starbursts there may be changes in the chemical composition of the ISM and dust due to the relative abundance of products from massive stars, enriching the ISM with O and producing a lower C/O ratio than normal. This may have the effect of reducing CO abundance as well as increasing O-rich dust species. If correct, this hypothesis implies that large deviations in the dust-CO or (dust-H_2) ratio must happen regularly in the life of intermediate mass, gas-rich galaxies, since BADGRS make up more than half of the galaxies in the H-ATLAS local volume survey, HAPLESS. As it is a dust mass-selected sample, HAPLESS would preferentially include galaxies near this hypothetical 'peak' in their dust cycle.

Alternatively, if we use instead the dust emission and theoretical arguments (Section 5.1; Table 5) to estimate Σ_{H_2} for BADGRS ($\Sigma_{H_2,d} = f_{H_2,th} \times \Sigma_g$), the SFE drops dramatically and the depletion times become similar to or longer than the more massive galaxies (grey circles in Fig 11).

In summary, either BADGRS have an enhanced SFE (short molecular depletion time-scale, $\tau_{dep} \sim 0.5$ Gyr) or, they have normal SFE with $\tau_{dep} \sim 2.4 - 4$ Gyr but some mechanism means that

[21] We find a similar τ_{dep} for the sample of late type spirals from the HRS when using the Wolfire et al. (2010) metallicity-dependent α_{CO} and the same sample as plotted in Fig. 8(b).

they are more deficient in CO relative to their H_2 content than the current understanding of metallicity scaling relations predict. Measuring the star formation histories across these galaxies to determine how much of an influence a bursty history might have will be possible using IFU data, to be presented in Ballard et al. (in preparation).

6 CONCLUSIONS

We have presented measurements of the ^{12}CO J = 1,2,3 lines for nine positions in four representative examples of extremely blue but dusty gas-rich galaxies (BADGRS) found in the first dust mass-selected sample from the *Herschel*-ATLAS survey.

(i) The CO lines in these sources are very weak with $T_p = 5-30$ mK (T_{mb}), the linewidths are narrow in some cases, and the implied $\Sigma_{H_2,CO} = 0.5 - 6\,M_\odot\,pc^{-2}$ is 6–10 times less than the inter-arm density in M51, averaged over a similar area.

(ii) The BADGRS exhibit a range of excitation conditions from their low-J CO lines, much the same as other local spirals.

(iii) Using a metallicity-dependent α_{CO}, we find M_{H_2}/M_d ratios of 7−27, which are a factor ∼10 lower than other local samples with consistently estimated metallicities, M_{H_2} and dust masses. The M_{H_2}/M_d ratio is found to be insensitive to metallicity.

(iv) The BADGRS have similar $M_{H_2}-M_*$ properties compared to other local samples, although the scatter in these relations is large.

(v) Using dust as a tracer of total gas surface density, we show that the average ISM pressure in the regions where CO is measured should be high enough that at least 50 per cent of the gas there is in molecular form. The H_2 fractions inferred in this way are on average 11 times higher than those indicated by the CO emission.

(vi) The IRX-β_{UV} relation for BADGRS is offset to redder UV colour for a given attenuation compared to local star-forming galaxies and starbursts. The majority (74 per cent) of BADGRS lie on or below an SMC-like dust attenuation law, and in this way are similar to $z \sim 5$ galaxies (Faisst et al. 2017).

(vii) The diffuse dust temperatures in the BADGRS are much colder (13–16 K) than in typical spirals or low metallicity dust-poor dwarfs (18–31 K). For the same dust properties, this would require an ISRF 10–20 times lower than the local solar neighbourhood value, however, the observed radiation surface densities are in fact equivalent to the solar neighbourhood value. In order to explain this discrepancy either a radically different dust geometry (clumpier) or different dust properties (size distribution, composition, opacity) compared to the Milky Way and other local galaxies is required.

(viii) Using the CO-based M_{H_2}, BADGRS are significantly offset from the K–S relation for local spiral galaxies, with shorter molecular gas depletion time-scales of ∼0.5 Gyr, even when using a metallicity-dependent α_{CO}. In this respect they are similar to low-metallicity BCD galaxies, which have bursty star formation histories. Analysis of their SEDs and optical spectra also suggests BADGRS are currently, or have recently, experienced bursts of star formation. There may be a link between this and a genuinely enhanced dust-to-molecular-gas ratio.

Future papers will describe the data from ongoing high-resolution Jansky-VLA and ALMA studies of the atomic and molecular ISM and from optical IFU imaging of the stellar properties and kinematics. From this full data set and with radiative transfer modelling of the galaxies, we will be able to remove some of the assumptions made here and address these intriguing options in turn to solve the mystery posed by the BADGRS.

ACKNOWLEDGEMENTS

Thanks to A. Faisst, L. Hunt, V. Villaneuva, and M. Grossi for their help in providing data points for literature samples, and to S. Schofield for Fig. 4. We thank Y. Mao, N. Bourne, M. Michalowski, and S. Viaene for helpful comments. LD and SJM acknowledge support from the European Research Council Advanced Investigator grant, COSMICISM and Consolidator grant, CosmicDust. IO, ZZ, and RJI acknowledge support from the European Research Council Advanced Investigator grant, COSMICISM. HLG and PC acknowledge support from the European Research Council Consolidator grant, CosmicDust. This work is based on observations carried out under project number 077-14 with the IRAM 30m telescope. IRAM is supported by INSU/CNRS (France), MPG (Germany), and IGN (Spain). The *Herschel*-ATLAS is a project with *Herschel*, which is an ESA space observatory with science instruments provided by European-led Principal Investigator consortia and with important participation from NASA. The H-ATLAS web-site is http://www.h-atlas.org. GAMA is a joint European-Australasian project based around a spectroscopic campaign using the Anglo- Australian Telescope. The GAMA input catalogue is based on data taken from the Sloan Digital Sky Survey and the UKIRT Infrared Deep Sky Survey. Complementary imaging of the GAMA regions is being obtained by a number of independent survey programmes including GALEX MIS, VST KIDS, VISTA VIKING, WISE, *Herschel*-ATLAS, GMRT, and ASKAP providing UV to radio coverage. GAMA is funded by the STFC (UK), the ARC (Australia), the AAO, and the participating institutions. The GAMA website is: http://www.gama-survey.org/. We acknowledge the usage of the HyperLeda database (http://leda.univ-lyon1.fr).

REFERENCES

Ahn C. P. et al., 2014, ApJS, 211, 17
Amorín R., Muñoz-Tuñón C., Aguerri J. A. L., Planesas P., 2016, A&A, 588, A23
Aravena M. et al., 2016, MNRAS, 457, 4406
Asplund M., Grevesse N., Sauval A. J., Scott P., 2009, ARA&A, 47, 481
Baldry I. K. et al., 2012, MNRAS, 421, 621
Barrera-Ballesteros J. K. et al., 2016, MNRAS, 463, 2513
Battisti A. J., Calzetti D., Chary R.-R., 2016, ApJ, 818, 13
Bauermeister A., Blitz L., Bolatto A., Bureau M., Teuben P., Wong T., Wright M., 2013, ApJ, 763, 64
Bekki K., 2014, MNRAS, 444, 1615
Bianchi L. et al., 2005, ApJ, 619, L71
Bigiel F. et al., 2011, ApJ, 730, L13
Bigiel F., Leroy A., Walter F., Brinks E., de Blok W. J. G., Madore B., Thornley M. D., 2008, AJ, 136, 2846
Bisbas T. G., Papadopoulos P. P., Viti S., 2015, ApJ, 803, 37
Bisbas T. G., van Dishoeck E. F., Papadopoulos P. P., Szűcs L., Bialy S., Zhang Z.-Y., 2017, ApJ, 839, 90
Blitz L., Rosolowsky E., 2006, ApJ, 650, 933
Bolatto A. D. et al., 2011, ApJ, 741, 12
Bolatto A. D., Wolfire M., Leroy A. K., 2013, ARA&A, 51, 207
Boquien M. et al., 2009, ApJ, 706, 553
Boquien M. et al., 2012, A&A, 539, A145
Boselli A. et al., 2010, PASP, 122, 261
Boselli A., Cortese L., Boquien M., 2014, A&A, 564, A65
Bot C. et al., 2010, A&A, 524, A52
Bot C., Helou G., Boulanger F., Lagache G., Miville-Deschenes M.-A., Draine B., Martin P., 2009, ApJ, 695, 469
Bothwell M. S. et al., 2014, MNRAS, 445, 2599
Bothwell M. S. et al., 2017, MNRAS, 466, 2825
Bothwell M. S., Maiolino R., Peng Y., Cicone C., Griffith H., Wagg J., 2016, MNRAS, 455, 1156

Bourne N. et al., 2013, MNRAS, 436, 479
Bourne N. et al., 2016, MNRAS, 462, 1714
Bouwens R. J. et al., 2016, ApJ, 833, 72
Braine J., Combes F., 1992, A&A, 264, 433
Buat V. et al., 2012, A&A, 545, A141
Carleton T. et al., 2017, MNRAS, 467, 4886
Casey C. M. et al., 2014, ApJ, 796, 95
Chabrier G., 2003, PASP, 115, 763
Ciesla L. et al., 2014, A&A, 565, A128
Clark C. J. R. et al., 2015, MNRAS, 452, 397
Colombo D. et al., 2014, ApJ, 784, 3
Corbelli E. et al., 2012, A&A, 542, A32
Cormier D. et al., 2014, A&A, 564, A121
Cormier D. et al., 2016, MNRAS, 463, 1724
Cortese L. et al., 2014, MNRAS, 440, 942
Cortese L., Boselli A., Franzetti P., Decarli R., Gavazzi G., Boissier S., Buat V., 2008, MNRAS, 386, 1157
da Cunha E., Charlot S., Elbaz D., 2008, MNRAS, 388, 1595
da Cunha E., Eminian C., Charlot S., Blaizot J., 2010, MNRAS, 403, 1894
Daddi E. et al., 2010, ApJ, 713, 686
Dale D. A., Helou G., 2002, ApJ, 576, 159
Dame T. M., Hartmann D., Thaddeus P., 2001, ApJ, 547, 792
de Jong T., Clegg P. E., Rowan-Robinson M., Soifer B. T., Habing H. J., Houck J. R., Aumann H. H., Raimond E., 1984, ApJ, 278, L67
De Looze I., Barlow M. J., Swinyard B. M., Rho J., Gomez H. L., Matsuura M., Wesson R., 2017, MNRAS, 465, 3309
De Vis P. et al., 2017a, MNRAS, 464, 4680
De Vis P. et al., 2017b, MNRAS, 471, 1743
De Vis P., 2016, PhD thesis, Ghent University, Ghent, Belgium
Devereux N. A., Young J. S., 1990, ApJ, 359, 42
Downes D., Solomon P. M., 1998, ApJ, 507, 615
Draine B. T. et al., 2007, ApJ, 663, 866
Draine B. T. et al., 2014, ApJ, 780, 172
Driver S. P. et al., 2011, MNRAS, 413, 971
Driver S. P. et al., 2016, MNRAS, 455, 3911
Dunne L. et al., 2009, MNRAS, 394, 1307
Dunne L., Eales S. A., 2001, MNRAS, 327, 697
Dunne L., Eales S., Edmunds M., Ivison R., Alexander P., Clements D. L., 2000, MNRAS, 315, 115
Dunne L., Eales S., Ivison R., Morgan H., Edmunds M., 2003, Nature, 424, 285
Eales S. et al., 2010, PASP, 122, 499
Eales S. et al., 2018, MNRAS, 473, 3507
Elmegreen B. G., 1989, ApJ, 338, 178
Elmegreen B. G., 1993, ApJ, 411, 170
Faisst A. L. et al., 2017, ApJ, 847, 21
Fanciullo L., Guillet V., Aniano G., Jones A. P., Ysard N., Miville-Deschênes M.-A., Boulanger F., Köhler M., 2015, A&A, 580, A136
Feldmann R., Hernandez J., Gnedin N. Y., 2012, ApJ, 761, 167
Fontani F., Giannetti A., Beltrán M. T., Dodson R., Rioja M., Brand J., Caselli P., Cesaroni R., 2012, MNRAS, 423, 2342
Foyle K. et al., 2012, MNRAS, 421, 2917
Frayer D. T. et al., 2008, ApJ, 680, L21
Gall C. et al., 2014, Nature, 511, 326
Galliano F. et al., 2011, A&A, 536, A88
Geach J. E., Smail I., Moran S. M., MacArthur L. A., Lagos C. d. P., Edge A. C., 2011, ApJ, 730, L19
Genzel R. et al., 2010, MNRAS, 407, 2091
Genzel R. et al., 2015, ApJ, 800, 20
Giovanelli R., Haynes M. P., Salzer J. J., Wegner G., da Costa L. N., Freudling W., 1995, AJ, 110, 1059
Glover S. C. O., Mac Low M.-M., 2011, MNRAS, 412, 337
Gomez H. L. et al., 2012, MNRAS, 420, 3557
Gordon K. D., Clayton G. C., Witt A. N., Misselt K. A., 2000, ApJ, 533, 236
Gratier P. et al., 2010, A&A, 522, A3
Grossi M. et al., 2016, A&A, 590, A27
Guthrie B. N. G., 1992, A&AS, 93, 255
Hao C.-N., Kennicutt R. C., Johnson B. D., Calzetti D., Dale D. A., Moustakas J., 2011, ApJ, 741, 124
Haynes M. P. et al., 2011, AJ, 142, 170
Helou G., 1986, ApJ, 311, L33
Heyer M. H., Carpenter J. M., Snell R. L., 2001, ApJ, 551, 852
Hopkins A. M. et al., 2013, MNRAS, 430, 2047
Huang M.-L., Kauffmann G., 2014, MNRAS, 443, 1329
Hughes T. M. et al., 2017, MNRAS, 468, L103
Hunt L. K. et al., 2015, A&A, 583, A114
Hunt L. K. et al., 2017, A&A, 606, 99
Hunter D. A., Gallagher J. S., III, Rice W. L., Gillett F. C., 1989, ApJ, 336, 152
Indebetouw R. et al., 2014, ApJ, 782, L2
Ivison R. J., Papadopoulos P. P., Smail I., Greve T. R., Thomson A. P., Xilouris E. M., Chapman S. C., 2011, MNRAS, 412, 1913
Jones A. P., Fanciullo L., Köhler M., Verstraete L., Guillet V., Bocchio M., Ysard N., 2013, A&A, 558, A62
Juvela M. et al., 2018, A&A, 612, 71
Kennicutt Jr. R. C., 1998, ApJ, 498, 541
Kennicutt R. C., Evans N. J., 2012, ARA&A, 50, 531
Kewley L. J., Ellison S. L., 2008, ApJ, 681, 1183
Koda J. et al., 2012, ApJ, 761, 41
Köhler M., Stepnik B., Jones A. P., Guillet V., Abergel A., Ristorcelli I., Bernard J.-P., 2012, A&A, 548, A61
Kong X., Charlot S., Brinchmann J., Fall S. M., 2004, MNRAS, 349, 769
Kuno N. et al., 2007, PASJ, 59, 117
Lee N. et al., 2017, MNRAS, 471, 2124
Lee C., Leroy A. K., Schnee S., Wong T., Bolatto A. D., Indebetouw R., Rubio M., 2015, MNRAS, 450, 2708
Leroy A. K. et al., 2009, AJ, 137, 4670
Leroy A. K. et al., 2011, ApJ, 737, 12
Leroy A. K. et al., 2013, AJ, 146, 19
Leroy A. K. et al., 2016, ApJ, 831, 16
Leroy A. K., Walter F., Brinks E., Bigiel F., de Blok W. J. G., Madore B., Thornley M. D., 2008, AJ, 136, 2782
Madden S. C. et al., 2013, PASP, 125, 600
Magdis G. E. et al., 2012, ApJ, 760, 6
Magdis G. E. et al., 2014, ApJ, 796, 63
Makarov D., Prugniel P., Terekhova N., Courtois H., Vauglin I., 2014, A&A, 570, A13
Mao R.-Q., Schulz A., Henkel C., Mauersberger R., Muders D., Dinh-V-Trung, 2010, ApJ, 724, 1336
Mao Y.-W., Kennicutt Jr. R. C., Hao C.-N., Kong X., Zhou X., 2012, ApJ, 757, 52
Mao Y.-W., Kong X., Lin L., 2014, ApJ, 789, 76
Martin P. G. et al., 2012, ApJ, 751, 28
Martinsson T. P. K., Verheijen M. A. W., Westfall K. B., Bershady M. A., Schechtman-Rook A., Andersen D. R., Swaters R. A., 2013, A&A, 557, A130
Mathis J. S., Mezger P. G., Panagia N., 1983, A&A, 128, 212
Matsuura M. et al., 2011, Science, 333, 1258
Meegan C. A., Fishman G. J., Wilson R. B., Horack J. M., Brock M. N., Paciesas W. S., Pendleton G. N., Kouveliotou C., 1992, Nature, 355, 143
Meyer M. J. et al., 2004, MNRAS, 350, 1195
Narayanan D., Groppi C. E., Kulesa C. A., Walker C. K., 2005, ApJ, 630, 269
Nishimura A. et al., 2015, ApJS, 216, 18
O'Brien J. C., Freeman K. C., van der Kruit P. C., 2010, A&A, 515, A62
Overzier R. A. et al., 2011, ApJ, 726, L7
Papadopoulos P. P., Pelupessy F. I., 2010, ApJ, 717, 1037
Papadopoulos P. P., Thi W.-F., Viti S., 2002, ApJ, 579, 270
Papadopoulos P. P., van der Werf P. P., Xilouris E. M., Isaak K. G., Gao Y., Mühle S., 2012, MNRAS, 426, 2601
Pettini M., Pagel B. E. J., 2004, MNRAS, 348, L59
Pety J., 2005, in Casoli F., Contini T., Hameury J. M., Pagani L., eds. SF2A2005: Semaine de l'Astrophysique Francais. EdP-Sciences, Les Ulis, France, p. 721
Planck Collaboration XI, 2014, A&A, 571, A11

Planck Collaboration XIX, 2011, A&A, 536, A19
Planck Collaboration XXII, 2011, A&A, 536, A22
Planck Collaboration XXIX, 2016, A&A, 586, A132
Reddy N. A., Erb D. K., Pettini M., Steidel C. C., Shapley A. E., 2010, ApJ, 712, 1070
Rémy-Ruyer A. et al., 2015, A&A, 582, A121
Riess A. G. et al., 2011, ApJ, 730, 119
Roman-Duval J. et al., 2010, A&A, 518, L74
Rowlands K. et al., 2014, MNRAS, 441, 1017
Saintonge A. et al., 2011, MNRAS, 415, 32
Sakamoto S., Hayashi M., Hasegawa T., Handa T., Oka T., 1994, ApJ, 425, 641
Sakamoto S., Hasegawa T., Hayashi M., Handa T., Oka T., 1995, ApJS, 100, 125
Sakamoto S., Hasegawa T., Handa T., Hayashi M., Oka T., 1997, ApJ, 486, 276
Sandstrom K. M. et al., 2013, ApJ, 777, 5
Sawada T. et al., 2001, ApJS, 136, 189
Schmidt M., 1959, ApJ, 129, 243
Schmidt M., 1963, Nature, 197, 1040
Schofield S., 2017, PhD thesis, Cardiff University, Cardiff, UK
Schruba A. et al., 2011, AJ, 142, 37
Scoville N. et al., 2014, ApJ, 783, 84
Scoville N. et al., 2016, ApJ, 820, 83
Scoville N. et al., 2017, ApJ, 837, 150
Shi Y., Armus L., Helou G., Stierwalt S., Gao Y., Wang J., Zhang Z.-Y., Gu Q., 2014, Nature, 514, 335
Siana B. et al., 2009, ApJ, 698, 1273
Skibba R. A. et al., 2011, ApJ, 738, 89
Smail I., Ivison R. J., Blain A. W., 1997, ApJ, 490, L5
Smith D. J. B. et al., 2012a, MNRAS, 427, 703
Smith M. W. L. et al., 2012b, ApJ, 748, 123
Solomon P. M., Downes D., Radford S. J. E., Barrett J. W., 1997, ApJ, 478, 144
Swinbank A. M. et al., 2011, ApJ, 742, 11
Takeuchi T. T., Yuan F.-T., Ikeyama A., Murata K. L., Inoue A. K., 2012, ApJ, 755, 144
Tamburro D., Rix H.-W., Leroy A. K., Mac Low M.-M., Walter F., Kennicutt R. C., Brinks E., de Blok W. J. G., 2009, AJ, 137, 4424
Tully R. B., Pierce M. J., Huang J.-S., Saunders W., Verheijen M. A. W., Witchalls P. L., 1998, AJ, 115, 2264
Valdivia V., Hennebelle P., Gérin M., Lesaffre P., 2016, A&A, 587, A76
Valiante E. et al., 2016, MNRAS, 462, 3146
Viaene S. et al., 2016, A&A, 586, A13
Villanueva V. et al., 2017, MNRAS, 470, 3775
Weiß A., Downes D., Henkel C., Walter F., 2005, A&A, 429, L25
Wild V., Kauffmann G., Heckman T., Charlot S., Lemson G., Brinchmann J., Reichard T., Pasquali A., 2007, MNRAS, 381, 543
Wilson C. D. et al., 2009, ApJ, 693, 1736
Wolfire M. G., Hollenbach D., McKee C. F., 2010, ApJ, 716, 1191
Yao L., Seaquist E. R., Kuno N., Dunne L., 2003, ApJ, 588, 771
Young J. S. et al., 1995, ApJS, 98, 219
Ysard N., Köhler M., Jones A., Miville-Deschênes M.-A., Abergel A., Fanciullo L., 2015, A&A, 577, A110
Zhu M., Papadopoulos P. P., Xilouris E. M., Kuno N., Lisenfeld U., 2009, ApJ, 706, 941
Zibetti S., Charlot S., Rix H.-W., 2009, MNRAS, 400, 1181

This paper has been typeset from a TEX/LATEX file prepared by the author.